remote sensing

MDPI

Article

Trailing Equatorial Plasma Bubble Occurrences at a Low-Latitude Location through Multi-GNSS Slant TEC Depletions during the Strong Geomagnetic Storms in the Ascending Phase of the 25th Solar Cycle

Ram Kumar Vankadara [1], Punyawi Jamjareegulgarn [2], Gopi Krishna Seemala [3], Md Irfanul Haque Siddiqui [4] and Sampad Kumar Panda [1,*]

[1] Department of ECE, KL Deemed to be University, Koneru Lakshmaiah Education Foundation, Guntur 522302, India; 2002040005@kluniversity.in
[2] Department of Electrical Engineering, Faculty of Engineering, King Mongkut's Institute of Technology Ladkrabang, Prince of Chumphon Campus, Chumphon 86160, Thailand; punyawi.ja@kmitl.ac.th
[3] Indian Institute of Geomagnetism, Navi Mumbai 410218, India; gopi.seemala@iigm.res.in
[4] Mechanical Engineering Department, College of Engineering, King Saud University, Riyadh 11451, Saudi Arabia; msiddiqui2.c@ksu.edu.sa
* Correspondence: sampadpanda@kluniversity.com or sampadpanda@gmail.com

Abstract: The equatorial plasma bubbles (EPBs) are depleted plasma density regions in the ionosphere occurring during the post-sunset hours, associated with the signal fading and scintillation signatures in the trans-ionospheric radio signals. Severe scintillations may critically affect the performance of dynamic systems relying on global navigation satellite system (GNSS)-based services. Furthermore, the occurrence of scintillations in the equatorial and low latitudes can be triggered or inhibited during space weather events. In the present study, the possible presence of the EPBs during the geomagnetic storm periods under the 25th solar cycle is investigated using the GNSS-derived total electron content (TEC) depletion characteristics at a low-latitude equatorial ionization anomaly location, i.e., KL University, Guntur (Geographic 16°26′N, 80°37′E and dip 22°32′) in India. The detrended TEC with a specific window size is used to capture the characteristic depletion signatures, indicating the possible presence of the EPBs. Moreover, the TEC depletions, amplitude (S4) and phase scintillation (σ_{φ}) indices from multi-constellation GNSS signals are probed to verify the vulnerability of the signals towards the scintillation effects over the region. Observations confirm that all GNSS constellations witness TEC depletions between 15:00 UT and 18:00 UT, which is in good agreement with the recorded scintillation indices. We report characteristic depletion depths (22 to 45 TECU) and depletion times (28 to 48 min) across different constellations confirming the triggering of EPBs during the geomagnetic storm event on 23 April 2023. Unlikely, but the other storm events evidently inhibited TEC depletion, confirming suppressed EPBs. The results suggest that TEC depletions from the traditional geodetic GNSS stations could be used to substantiate the EPB characteristics for developing regional as well as global scintillation mitigation strategies.

Keywords: equatorial plasma bubble; multi-GNSS constellations; ionospheric irregularities and scintillation; TEC depletion; geomagnetic storm

Citation: Vankadara, R.K.; Jamjareegulgarn, P.; Seemala, G.K.; Siddiqui, M.I.H.; Panda, S.K. Trailing Equatorial Plasma Bubble Occurrences at a Low-Latitude Location through Multi-GNSS Slant TEC Depletions during the Strong Geomagnetic Storms in the Ascending Phase of the 25th Solar Cycle. *Remote Sens.* **2023**, *15*, 4944. https://doi.org/10.3390/rs15204944

Academic Editors: Lei Liu, Zihan Wang, Yunbin Yuan and Jun Wang

Received: 16 September 2023
Revised: 9 October 2023
Accepted: 11 October 2023
Published: 13 October 2023

1. Introduction

The equatorial plasma bubbles (EPBs) are the regions of depleted electron density in the post-sunset equatorial and low-latitude ionosphere surrounded by enhanced electron density areas, leading to ionospheric electron density irregularities with scale sizes ranging from a few meters to thousands of kilometers [1–5]. Based on horizontal scale sizes, the EPBs are generally classified as large (>100 km), intermediate (10 km–100 m), and small (<100 m) scale structures, respectively [6]. Irregularities in the intermediate range constitute

an important part of EPBs and primarily affect the very high-frequency (VHF) radio waves whereas those in the small-scale ranges are responsible for the disturbances in the L-band transmissions. There is a particular interest in the characteristics of these irregularity scale lengths as it may critically affect the operation of satellite-based communication and navigation systems by introducing degraded signal strengths or even loss of lock [7]. Plasma irregularities and depletions associated with EPBs are generally observed during the nighttime, shortly after sunset, and may even persist until a few hours after midnight. The general morphology of EPBs including the source mechanism, evolution processes, spatial structures, and global distributions have been presented in the past through ground- and satellite-based observations. From the analysis of these observations, it has been established that the EPBs are often initiated in the post-sunset hours under the action of pre-reversal enhancement (PRE) in zonal electric field by suddenly uplifting plasma to a higher altitude with a steep plasma density gradient in the bottomside F-layer. This favors the growth of the irregularities by the Rayleigh–Taylor instability (RTI) in the bottomside ionosphere and their subsequent transportation to topside ionosphere and higher latitudes along the magnetic field tubes [8–12]. The eastward post-sunset electric field enhances the RTI, while the westward electric field may suppress the instability. The structures that form due to this instability can grow to become large-scale ionospheric depletions, often called equatorial plasma bubbles. The variability due to the uplift of the F-layer after sunset by the PRE may dictate the onset or inhibition of these ionospheric depletions [12,13]. Radio wave propagation, satellite communication, and Global Navigation Satellite System (GNSS) signals are substantially affected by the EPBs, making them of great interest to researchers in the field of space weather and ionospheric physics.

Although the spatiotemporal occurrence distributions of EPBs are strongly controlled by local time, season and geographic location of observation, they are often driven by the disturbances of solar origin such as solar flares, coronal mass ejections, geomagnetic storms, etc. [14,15]. The plasma density irregularities within the EPBs can scatter and diffract the traversing radio waves, causing abrupt fluctuations in the amplitude (amplitude scintillation) and phase (phase scintillation) of the received signal. Based on the severity, the scintillations can interrupt or degrade GNSS receiver operation by potentially introducing fading, cycle slips, ranging errors or even loss of tracking and may take considerable amount of time for reacquisition [16]. Further, during extreme space weather events, the probability of failures in measurements of GNSS navigational parameters increases and the positioning error could increase up to 10 times compared to its quiet time background level [17]. The significant magnitude of TEC gradients associated with the inner edges (very steep with large magnitudes) or the plasma density irregularities in the interior (lesser magnitude but more prevalent) of the bubble could potentially cause malfunctioning of GNSS receivers by affecting the functional accuracy and reliability [18–20]. Although there are progressive results on the ionospheric irregularities and loss of lock mechanism in the past, the complex origin and the dynamics of the ionospheric irregularities relevant to their effects on GNSS and communication systems are not yet fully understood. Using data from the European Space Agency (ESA) Swarm mission, De Michelis et al. [21,22] inferred that plasma bubbles certainly exhibit scaling properties that are associated with large density gradients arising from the turbulent nature of the irregularities. Their studies suggest that the turbulent characters are reflected in the high rate of change in electron density index (RODI) values inside bubbles. Pezzopane et al. [23] highlighted that the GNSS loss of lock events is strongly correlated with well-defined values of both RODI and the rate of change in the TEC index (ROTI), suggesting their origin in the regions with high electron density gradients. Recent investigation of De Michelis et al. [20] on loss of lock events using long-term Swarm observations reported that the GNSS loss of lock is very often confined to the turbulent plasma density irregularities with intermittent structures and extremely high RODI.

Detecting EPBs is a challenging task as they are dynamic and often exhibit complex spatial and temporal characteristics. An EPB may travel across different longitudes and

change its shape and strength of irregularities before diminishing in the background electron density [24]. Post-event detection methods provide us with a detailed description of bubble characteristics like bubble depth, bubble occurrence period, and the impact of the bubble on TEC depletion. Numerous techniques have been developed to detect EPBs using data from ground-based instruments, Radar observations [25], ionogram analysis [26], airglow data [10], and Global Navigation Satellite Systems (GNSS) [27–29] which include Global Positioning System (GPS), European Global Navigation System (Galileo), Russian Global Navigation Satellite System (GLONASS), Quasi-Zenith Satellite System (QZSS), Satellite-Based Augmentation System (SBAS), Chinese BeiDou Navigation Satellite System (BeiDou) [30,31]. Kelly et al. [32] first observed the EPBs using the RADAR data as the plumes or wedges. The ionograms describe the presence of EPB as the equatorial spread F phenomenon in the ionospheric F layer [33]. The all-sky imager captures the night airglow in the optical imager 630 nm images in which the dark bands or intensity-depleted regions are the signatures of EPBs [5].

Continuous observational data of the F-region anomaly were observed in Sanya from 2009 to 2010 at the equinox months using VHF radar data, GPS observations, and ionosonde observations [34]. The results indicated that the observed field alignment irregularities, scintillation values, and TEC depletion may be related to the possible development of EPB. Nakata et al. [35] used the 630 nm airglow data from the visible light and infrared spectrum imager to identify the EPBs. The electron density inside the EPB decreases, which is visible as a dark patch in the airglow image, considering it as an EPB occurrence. The EPBs marked in the airglow data are in line with the EPB occurrence observed through the ionosonde and GPS observations. Studies on EPB occurrence based on GNSS-derived TEC depletion or ROTI are emphasized nowadays as there exists a direct relationship between the ROTI, irregularity strength, and scintillation indices [19]. Zakharenkova and Cherniak [36] highlighted the strong connection between phase fluctuation intensity specified by ROTI and degradation in precise GPS during an extreme EPB prevailing condition. Astafyeva et al. [37] analyzed the global ROTI maps along with data from other ground- and space-based observations during geomagnetic storm to present a global multi-instrumental overview of ionospheric TEC and electron density irregularities during the storm. It shows that a relatively denser coverage of global ROTI datasets from a huge infrastructure of conventional geodetic GNSS receivers than any other ground-based monitoring units across the globe appeals exploitation of TEC depletion strengths and ROTI for understanding long-term global morphology of EPBs [38–41]. TEC or slant total electron content (sTEC) is the number of electrons present in the ray path between the satellite and the receiver measured in TECU where 1 TECU = 10^{16} electrons/m^2 [42]. Magdaleno et al. [13] used the sTEC data obtained from the GPS satellites at six stations all over the world to find the plasma bubble occurrence. The model response at different seasons and temporal variations was observed. The in-depth analysis showed a TEC depletion ranging from 6 TECU to 18 TECU from all the stations. Portillo et al. [14] collected the sTEC values every 10 min to find out the plasma bubble formation in the equatorial Africa region for the early 6 months of 2004. The results show that the average plasma bubble depletion depth is 9 TECU while the average apparent depletion time is 90 min. Mersha et al. [38] used the sTEC data from high-rate GNSS receivers at African GNSS stations in 2014 and 2015 to verify the possible EPB occurrence. The preliminary observations in the TEC detrended curve showed the characterization depth of EPB ranging from 10 TECU to 40 TECU, and the depletion time ranging from 15 to 68 min. Nishioka et al. [39] used data from 23 GPS receivers along the dip equator to verify the plasma bubble occurrences from 2000 to 2006. Their observations from the monthly occurrence rates of the EPB in all the longitudinal stations emphasize that sunset time lag played a crucial role in the evolution of EPBs. With the introduction of a greater number of low earth orbiting (LEO) satellites, a great opportunity was provided for studying the global spatiotemporal features of EPBs and ionospheric irregularities from using onboard high resolution magnetic field measurements, GNSS radio occultation (RO) or Langmuir probe (LP) measurements which can address the

limitations of sparse coverage from ground-based observations up to some extent. Unlike other available constellations, the special configuration in Swarm constellation provides an opportunity for investigating the plasma irregularities in both meridional and zonal directions for understanding their relationship with plasma depletion and transient loss of lock in GNSS signals [43]. Cherniak et al. [44] conducted a multi-instrumental analysis with F3/C1 RO electron density profiles and scintillation indices along with in situ plasma probe observations from C/NOFS, Swarm, and DMSP satellites to characterize development of the storm induced EPBs and scintillation effects. Global DMSP profiles of plasma densities during the high solar activity periods detects the post-sunset variation of electric fields in the equatorial ionosphere, which is the source of increased occurrence of EPBs as closely aligned magnetic field lines with the terminator favors the formation of bubbles [45]. Unlike other ground-based or LEO observations, with the two-dimensional images of the equatorial and low-latitude ionosphere taken by Global-scale Observations of the Limb and Disk (GOLD) imager from geostationary orbit provide scopes for unambiguous measurement of the formation, drifting direction, and evolution of EPBs on a global scale morphology [46]. Martinis et al. [47] investigated the longitudinal discrepancies in the onset time and occurrence rate of plasma depletions using GOLD data, demonstrating that the depletions can occur an hour or more after the onset of EPBs depending on the season and longitude of observation. Results of Cai et al. [48] reported that EPBs are clearly discernable in the GOLD nighttime OI 135.6 radiance and may serve as reference for identifying its link with TEC depletion as observed by GNSS-based measurements. Recent work of Karan et al. [49] pointed out the unusual appearance of differently shaped EPBs within a narrow longitude range using GOLD data. This could be due to small-scale longitudinal discrepancies in the electric field, E-layer electron density, alterations in neutral wind, or an amalgamation of these parameters. Concurrent investigation of GOLD and ionosonde observations to determine EPB occurrence rate and EIA morphology over an extended longitude region have been performed during the 23–29 September 2020 geomagnetic storm [50]. Statistical analysis of GOLD observations resulted in a significant knowledge on EPB climatology, its periodicity (3 and 6 days), and inverse geomagnetic activity dependencies during various phases of storms [51].

The development of EPBs can be modulated or inhibited depending on the orientation and strength of the ionospheric electric fields, the regular characteristics of which are modified during the magnetically disturbed periods. The consequences, however, can be very confined and vary from storm to storm and location to location. Earlier researchers have reported the presence of enhanced [52–55] or suppressed [56,57] scintillations/EPBs during different geomagnetic storms. Their studies suggest relatively stronger E $\times$ B vertical drifts in the local evening sector due to the superposition of storm-induced eastward penetrating electric fields with the regular electric fields to favor RTI manifestation. Conversely, Nayak et al. [56] showed a clear absence of scintillation over the anomaly crest region station Pingtung, Taiwan during the St. Patrick's Day geomagnetic storm (17 March 2015). Dugassa et al. [57] also conducted a regional study over American, African and Indian longitudinal sectors where the Indian sector exhibited the storm inhibition characteristics in five major geomagnetic storms of the equinoctial months during 2012–2013. The suppression in scintillation is due to westward penetrating electric fields and disturbance dynamo electric fields which creates an unfavorable scenario for RTI manifestations by bringing down the altitude of PRE [58,59]. Further studies on the ROTI parameters along the Asian longitudes during different equinoctial geomagnetic conditions reveal triggering and suppression effects of EPBs during the main and recovery phases, respectively [60]. Tulasi Ram et al. [61] employed multi-instrumental (ground-based and spaceborne) and multi-station data to study the onset and suppression of ionospheric perturbations across large longitude sectors during moderate to severe geomagnetic storms. The results show that the enhancement (suppression) of the EPBs varies with the onset of the storm and eastward (westward) penetrating electric fields. Further, modeling studies of Sripathi et al. [62] emphasize the role of penetration electric fields in the enhancement or suppression of the EPBs around the

global equatorial belt. Although most extreme scintillation activity is expected to occur near the equatorial region during geomagnetic storms, the severity of the scintillations may vary depending on the onset time of the storm and phase of the storm (main or recovery) [52,62]. Despite many studies, the occurrence of equatorial plasma bubbles during magnetic storms has not been fully understood.

Concerning the frequency of scintillation activity at the geographic location of the present study, Brahmanandam et al. [63] conducted a campaign mode study earlier in November 2011, confirming intense scintillation scenarios on 6 November 2011 that instigated the ionospheric group to exploit TEC irregularities and scintillation indices at the location with the establishment of a GNSS ionospheric scintillation and a TEC monitor (GISTM) receiver at KL University, Guntur, India (Geographic 16°26′N, 80°37′E and dip 22°32′). The recordings from this monitoring unit report weak to strong scintillation activities at times, associated with a specific number of GNSS satellite signals [64–67]. Considering the importance of the location, a modern multi-constellation and multi-frequency GISTM receiver (Septentrio-PolaRx5S) has been established recently in the year 2021 that records the slant TEC from all the available constellations along with the scintillation indices and several other parameters [68]. Preliminary observations from this high-end monitoring unit confirmed instances of scintillations and loss of lock scenarios due to intense scintillation activity in October 2022 [69–71]. However, most of the earlier investigations conducted at this particular location are based on observation, modeling and forecasting of GPS scintillation indices and belong to the previous solar cycle, i.e., Solar cycle 24. To the best of our knowledge, the multi-constellation scintillation indices and TEC depletion characteristics are barely explored at this location.

Hence, in this work, we focus on probing the presence of EPBs over the present location by analyzing the satellite to the receiver slant TEC (sTEC) depletions as well as phase and amplitude scintillation indices across multi-constellation and multi-frequency GNSS signals prevailing during the most geomagnetically disturbed days (Dst < −100 nT) under the 25th solar cycle. It involves addressing the influence of geomagnetic storms on EPBs in the equinoctial storm days when the regular EPB occurrences prevail over low latitudes. Our results revealed the strengthening of EPBs on the 23 April 2023 storm event amongst the three most disturbed equinoctial geomagnetic periods considered in this study by substantiating the relationship between TEC depletion and scintillation intensities across multi-constellation and multi-frequency GNSS signals which are discussed in detail in the rest of the sections. Section 2 provides Materials and Methods, and Section 3 provides Results and Discussion followed by Summary and Conclusions in Section 4.

2. Materials and Methods

The total electron content (TEC), amplitude scintillation index (S4) and phase scintillation index (σ_φ) data used in this study are obtained from the GNSS ionospheric scintillation and TEC monitoring (GISTM) multi-constellation, multi-frequency GNSS receiver (Septentrio make PolaRx5S) established at a low-latitude location, KL University, Guntur, India (Geographic 16°26′N 80°37′E, dip 22°32′). The raw data recorded by the receiver at a 50 Hz frequency is converted to ionospheric scintillation monitoring record (ISMR) format that contains the TEC values every 15 s along with many other parameters including scintillation indices, time of the week, elevation angle, azimuth angle, etc., for every minute. To validate the TEC values recorded by the GISTM receiver, we employ the recorded RINEX observation files in an alternative TEC calculation software, such as TayAbsTEC [72–74] and GPS-TEC analysis [75]. It is observed that the results are quite comparable to the GISTM recordings with GPS-TEC analysis plots apparently coinciding with the recorded TEC outputs. The signal combinations and satellite biases handled by the GISTM receiver for each constellation to determine TEC are presented in Table 1. The station biases corresponding to the antenna, connecting cable, and receiver are routinely calibrated against SBAS for better accuracy. In brief, the TEC is measured from P-code measurements, whereas the dTEC is computed from the carrier phase measurements only. On the contrary, in GPS-TEC

analysis, the satellite differential code biases (DCBs) are taken from IGS CODE files and receiver biases are estimated by itself, whereas TayAbsTEC estimates both of the biases independently for determining TEC. It is worth mentioning that in the present case, the detrending method is used in the individual PRN signals for calculating TEC depletion assuming that the common receiver-specific errors are eliminated in the analysis and hence no external calibration is involved in this study. Table 1 shows the available signals from various GNSS constellations and their combinations used by the PolaRx5S receiver unit for estimating scintillation indices and TEC, respectively. At present, the station records data for GPS, Galileo, and BeiDou at three available frequencies, GLONASS and GAGAN at two frequencies, and Navigation with Indian Constellation (NavIC) at only one frequency. In the present study, we do not include NavIC and GAGAN constellations for the TEC variable as NavIC records data only in L5, whereas TEC recorded by the latter is uncorrected with biases. In the present study, we select four geomagnetically disturbed days (see Table 2) in the ascending phase of the 25th solar cycle with a typical threshold of disturbance storm index (Dst) < −100 nT for analyzing the triggering/suppression of EPBs through signatures of TEC depletion and scintillation indices in the GNSS signals. The associated interplanetary magnetic field (IMF Bz) as well as geomagnetic ap index (ap), and Kp indices downloaded from the Omni Web-NASA server (https://omniweb.gsfc.nasa.gov/form/dx1.html, accessed on 5 August 2023) are also explored for a clear understanding of the onset and evolution of the storms.

Table 1. The available frequencies and signal combinations used in the PolaRx5S receiver monitoring unit established at KL University, Guntur, India for scintillation indices and TEC retrievals under different GNSS constellations.

S.No.	GNSS Constellation (RINEX Symbols)	Available Frequencies (GHz) for Scintillation Indices			Signal Combinations for TEC
		Signal 1	Signal 2	Signal 3	
1	GPS (G)	L1 (1.57)	L2 (1.22)	L5 (1.17)	L1P-L2P
2	GLONASS (R)	L1 (1.60)	L2 (1.24)	NA	L1CA-L2CA
3	Galileo (E)	E1 (1.57)	E5a (1.17)	E5b (1.20)	E1-E5a
4	BeiDou (C)	B1 (1.56)	B3 (1.26)	B2 (1.20)	B1-B2
5	GAGAN (S)	L1 (1.57)	NA	L5 (1.17)	L1CA-L5
6	IRNSS/NavIC (I)	NA	NA	L5 (1.17)	NA

Here, NA implies not applicable; the GAGAN TEC is not included as the bias is uncorrected and NavIC TEC is not recorded by the receiver as only one frequency (L5) is available.

Table 2. The extreme values for the geomagnetic indices (IMF Bz, Dst, ap, and Kp) for the strong storm days in the ascending phase of the 25th solar cycle.

S. No	Geomagnetic Indices	27 February 2023	23 March 2023	24 March 2023	23 April 2023
1	IMF Bz (nT)	6.7	0.3	4.6	21.7
2	Dst (nT)	−132	−126	−156	−165
3	ap (nT)	94	94	94	56
4	Kp	6.7	7	8	8.3

The presence of bubbles is discovered by monitoring the sudden fall in TEC revealed in the detrended TEC curve. The detrended TEC curve is obtained by subtracting the observed TEC from its moving average with a specific window size which determines the number of observations required to calculate the moving average. Earlier studies used different window sizes like 10 min [13,76,77], 60 min [38], and 91 min [14], based on the location and resolution of the input data. We also try a 120 min window size to check for the fitting of the detrended TEC for possible plasma bubble detection. All 4 window sizes are used to obtain the detrended TEC curves as shown in Figure 1 (upper panels).

To ensure that the depletion is due to plasma bubbles and not because of ionospheric shift perturbations or any bias in the data, we impose thresholds on the depletion curve characteristics [14]. The TEC depletion depth Δ(sTEC) ≥ 10 TECU, the apparent duration (t_{sTEC}) of the depletion should be 10 < t_{sTEC} < 180 min, the absolute minimum of the TEC depletion should be ≥5 TECU, and the maximum value of detrended TEC across the left and right side of the depletion ≥5 TECU. Δ(sTEC) is defined as the difference between the minimum value of the detrended TEC curve and the mean of the maximum left and right of the depletion value. The t_{sTEC} is the time taken by the depletion depth and is the difference between the times of maximum value on the right and left of the depletion. To demonstrate the retrieval of TEC depletion parameters through employing different moving average window sizes, we show the sTEC, its moving average and detrended sTEC for a specimen GNSS signal (PRN 32 of GPS and PRN 89 of Galileo constellations) in Figure 1. From our observations, it is realized that the 60 min window size is the most suitable candidate for inferring the TEC depletion characteristics coping with the plasma bubble criteria. The 10 min window size underfits the TEC detrended curve, with shallow TEC depletions that relate to the medium-scale travelling ionospheric disturbances (MSTIDS) and lower atmospheric gravity waves [77,78]. The 90 min and 120 min window sizes overfit the data and include some of the depletions with more values of depletion depth and depletion duration from the plasma bubble criteria. The window size with the 60 min moving average is best suited for both shorter and longer plasma bubble operations.

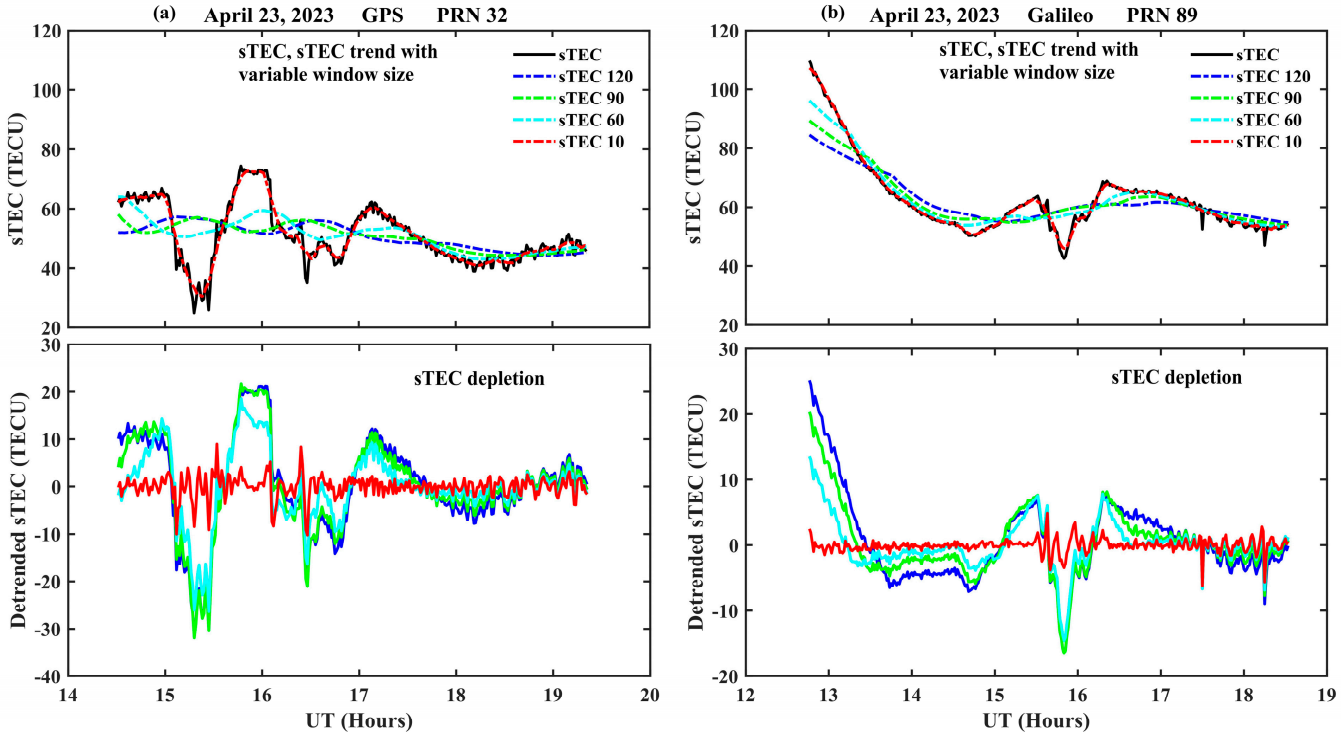

Figure 1. Detrending sTEC to determine depletion in (**a**) PRN 32 (GPS) and (**b**) PRN 89 (Galileo) on 23 April 2023. The upper panels show observed sTEC (black) and sTEC trend with variable window sizes (10 (cyan), 60 (red), 90 (green), and 120 (blue) minutes). The lower panels show detrended sTEC (sTEC depletion) in respective PRNs.

In Figure 2 (upper panel), we show the sTEC (black line) for PRN 32 of GPS and PRN 89 of Galileo constellations along with the 60 min moving average (blue line) and their detrended TEC (red line with marker 'x'). The zoomed-in version of respective depletions (red line with marker 'x') indicating the calculation of depletion depth (Δ(sTEC)) and its apparent duration (t_{sTEC}) is presented in Figure 2 (lower panel). A zero line (dark grey) is drawn in this figure to differentiate the positive and negative values in the detrended TEC curve.

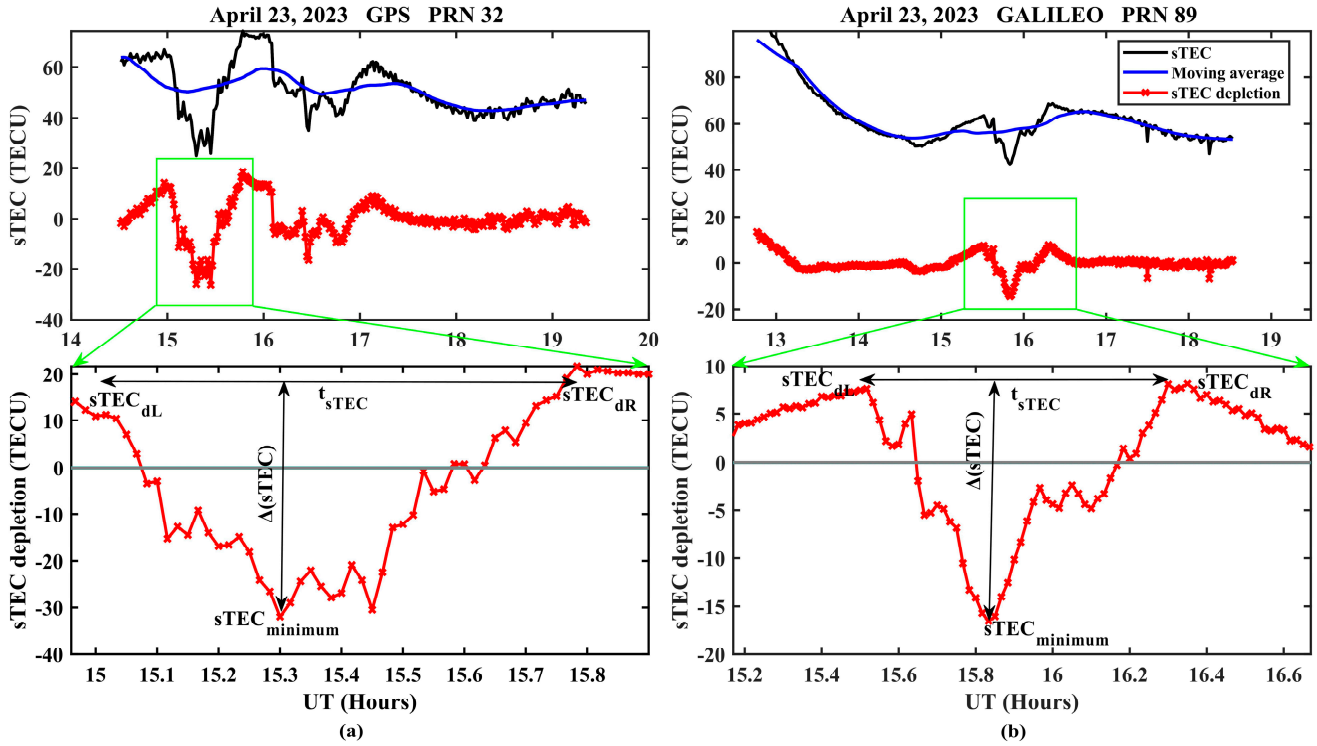

Figure 2. The observed sTEC (black line), moving average (blue line) and the detrended TEC curves (sTEC depletion; red line with a marker 'x') for (**a**) PRN 32 (GPS) and (**b**) PRN 89 (Galileo) in the upper panels, followed by the zoomed-in versions of the region of interests in lower panels, indicating the respective TEC depletion depth (Δ(sTEC)) and apparent duration (t_{sTEC}) during the geomagnetic storm event on 23 April 2023.

The depletion depth (Δ(sTEC)) is calculated as in Equation (1):

$$\Delta(\text{sTEC}) = \text{abs}(\text{sTEC}_{\text{minimum}}) + \frac{\text{sTEC}_{\text{dL}} + \text{sTEC}_{\text{dR}}}{2}, \quad (1)$$

where $\text{sTEC}_{\text{minimum}}$ is the minimum value in the detrended TEC curve, sTEC_{dL} and sTEC_{dR} are the nearby maximum values on the left and right of the absolute minimum value in the detrended TEC curve as shown in Figure 2b. The apparent duration or the depletion time (t_{sTEC}) is calculated as in Equation (2).

$$t_{sTEC} = \text{UT}(\text{sTEC}_{\text{dR}}) - \text{UT}(\text{sTEC}_{\text{dL}}), \quad (2)$$

where UT (sTEC_{dL}) is the time at the sTEC_{dL}, and UT (sTEC_{dR}) is the time at the sTEC_{dR} in the TEC detrended curve as shown in Figure 2b. PRNs from all the GNSS constellations fulfilling the threshold values for the indication of plasma bubble occurrence are chosen in this study. TEC depletion is observed in some PRNs that do not fulfil the thresholds of possible plasma bubble occurrence. This depletion may be due to the F layer anomalies, ionospheric density redistribution or MSTIDs. Further, the ionospheric delays corresponding to the frequencies are calculated using the sTEC depletions for the satellite PRNs affected by the EPB.

The ionospheric delays corresponding to the depletion depth in any radio signal can be obtained by using Equation (3).

$$\text{I} = \frac{40.31071}{\text{f}^2} * \Delta(\text{sTEC}) \quad (3)$$

where 'I' denotes the ionospheric delay in meters, Δ(sTEC) is depletion depth in TECU, and f is the frequency of the radio signal in Hz.

In this study, the sTEC is used in all the computations and observations which is sometimes mentioned as TEC. The effect of the EPB on the other available frequencies of all the constellations is observed in terms of S4 and σ_{φ} that are recorded by the GISTM receiver along with observational TEC. To further substantiate the connection between TEC depletion at the location and prevailing EPBs over the Indian longitude sector on 23 April 2023 geomagnetic storm day, the ROTI variations at the present location (KLEF) and the available geodetic GNSS stations under International GNSS Service (IGS) stations (IISC, HYDE, and LCK3), ranging from near equatorial latitude to outer edge of equatorial ionization anomaly (EIA) crest latitude, are obtained from SIMuRG: System for Ionosphere Monitoring and Research from GNSS [79].

3. Results and Discussion

The possible plasma bubble occurrences for selected geomagnetically disturbed days, whose Dst index (Dst < −100 nT) falls in the category of strong geomagnetic storms under the ascending phase of Solar cycle 25, are investigated using the sTEC depletion characteristics. Based on the above criteria, only four storm days, namely 27 February, 23 and 24 March and 23 April 2023 (referring to three geomagnetic storm events), are chosen for analysis in this study [80]. Figure 3 presents the variation of interplanetary and geomagnetic indices (IMF Bz, Dst, ap, and Kp) for the chosen storm days. All selected days show a high Kp value (Kp > 5) with an increased ap (ap > 90 nT) except for April 23 which presents the highest ap index (ap = 56 nT). Lan et al. [81] showed that some days with ap <50 nT showed strong ionospheric irregularities. The Dst is also reported to be less than −100 nT on all days, suggesting strong geomagnetic storms [82]. April 23 recorded the lowest Dst (−165 nT) of all the disturbed days. Earlier research showed an increase in the occurrence probability of EPBs with magnetic activity wherein the main phase of the storm coincides with the local dusk time, thereby uplifting the F layer plasma through penetrating eastward electric fields and facilitating the RTI development [54,83]. However, some studies revealed the magnetic activity inhibiting the occurrence of the EPBs in the presence of disturbance dynamo electric fields (DDEFs) and westward electric fields, forcing the F layer electron density downward [58,84]. It can be marked that the IMF Bz variance is higher (22 nT) on 23 April than on the other days, suggesting that a sudden change in its polarity can manipulate the equatorial electric fields for triggering the pre-reversal enhancement (PRE) scenario that seeds the formation of EPBs [42,85]. The extreme values of all the geomagnetic indices for the storm days are given in Table 2.

The σ_{φ}, S4, and sTEC for all the available constellations of the storm day, the preceding day, and the successive day for the three storm events (27 February, 23, 24 March, and 23 April) are presented in Figures 4–6, respectively. We observe a severe scintillation activity in terms of high S4 and σ_{φ} on the 23 March and 23 April 2023 storm days. It is also evident that during all the storm days, the pre- and post-storm periods presented high scintillation activity in terms of S4 and σ_{φ} except for the 24 March and 23 April post-storm periods. Although there is a high geomagnetic activity observed in all the storm days (see Figure 4), the scintillation activity is suppressed in the 27 February and 24 March (Figures 5 and 6) storm days compared to pre- and post-storm periods. The possible reasons for the suppression of the scintillation are due to the reduction in the F layer height due to westward prompt penetration or the disturbance dynamo electric fields (PPEFs/DDEFs) reducing the PRE which is responsible for the possible plasma bubble manifestation and thereby enhancing the scintillation activity. The role of PPEF or DDEF during the geomagnetic storm to trigger/suppress EPBs by manipulating the zonal electric field is summarized in the earlier literature [7].

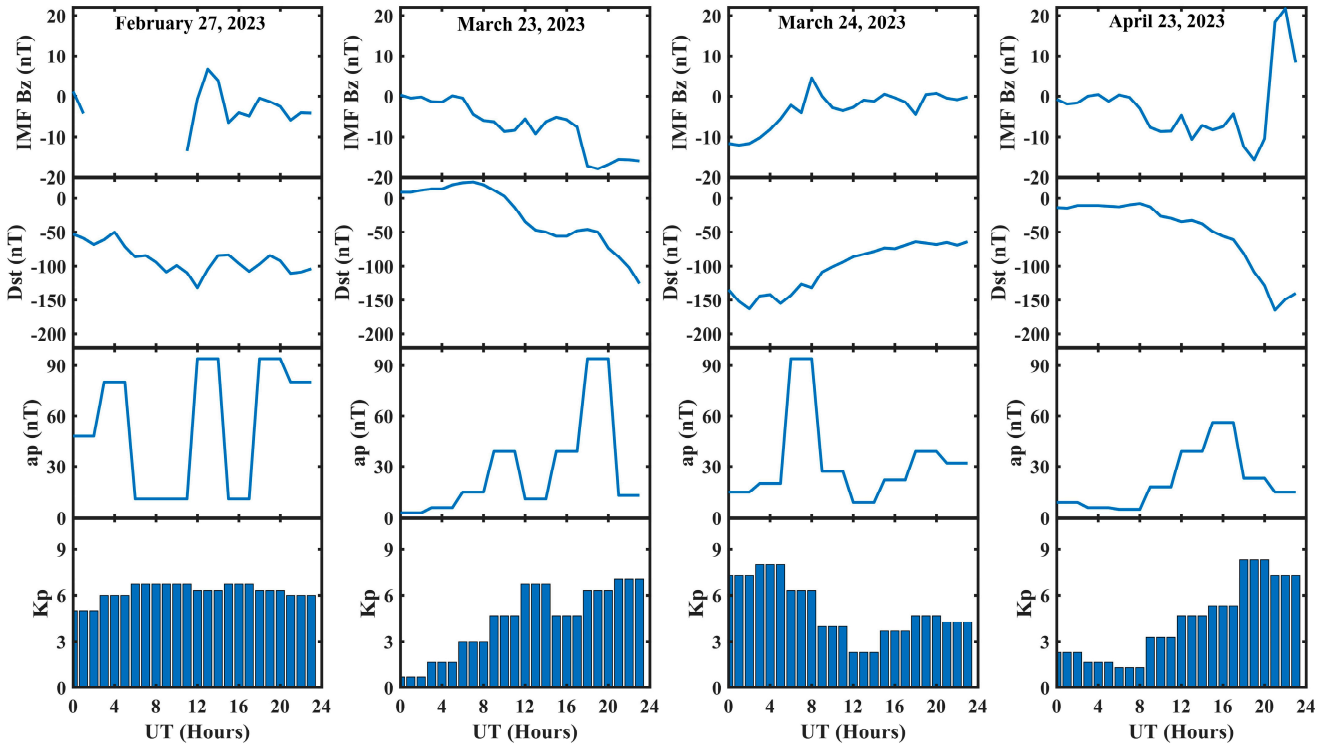

Figure 3. The IMF Bz, Dst, ap and Kp values for the storm days of 27 February, 23 and 24 March, and 23 April during the year 2023 from top to bottom.

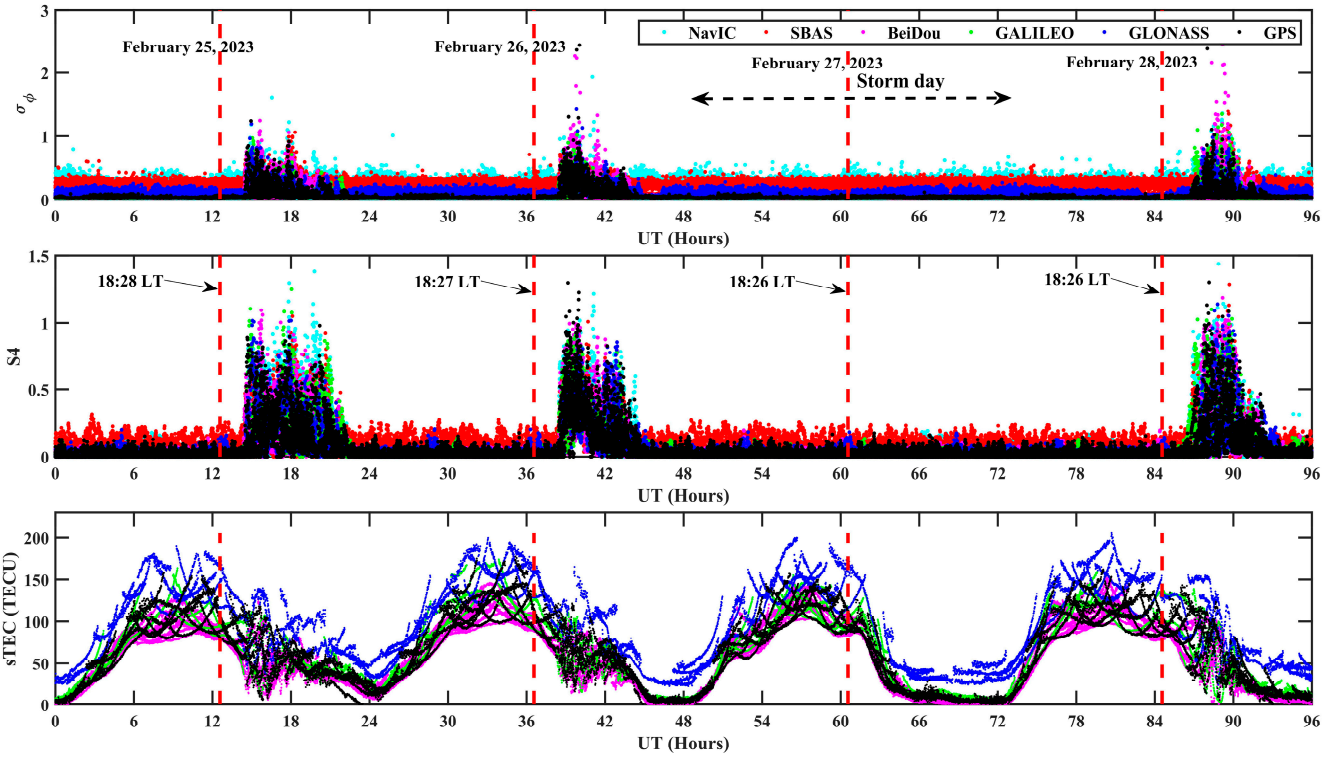

Figure 4. The σ_φ (**top panel**), S4 (**middle panel**) and sTEC (**bottom panel**) from all the available constellations on the days before the storm (25 and 26 February), during the storm (27 February), and after the storm (28 February) in 2023. The red dashed line shows the local sunset terminator for the above days.

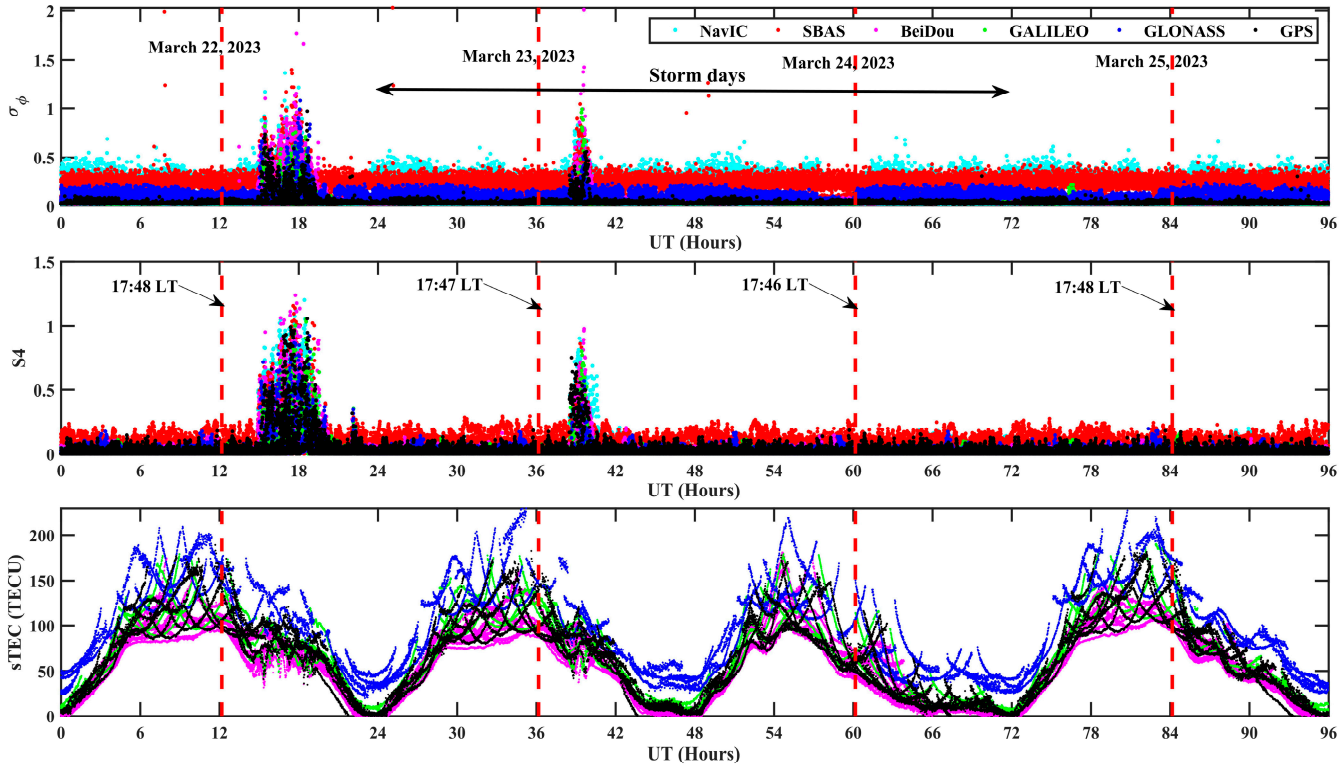

Figure 5. The σ_φ (**top panel**), S4 (**middle panel**) and sTEC (**bottom panel**) from all the available constellations on the days before the storm (22 March), during the storm (23, 24 March) and after the storm (25 March) in 2023. The red dashed line shows the local sunset terminator for the above days.

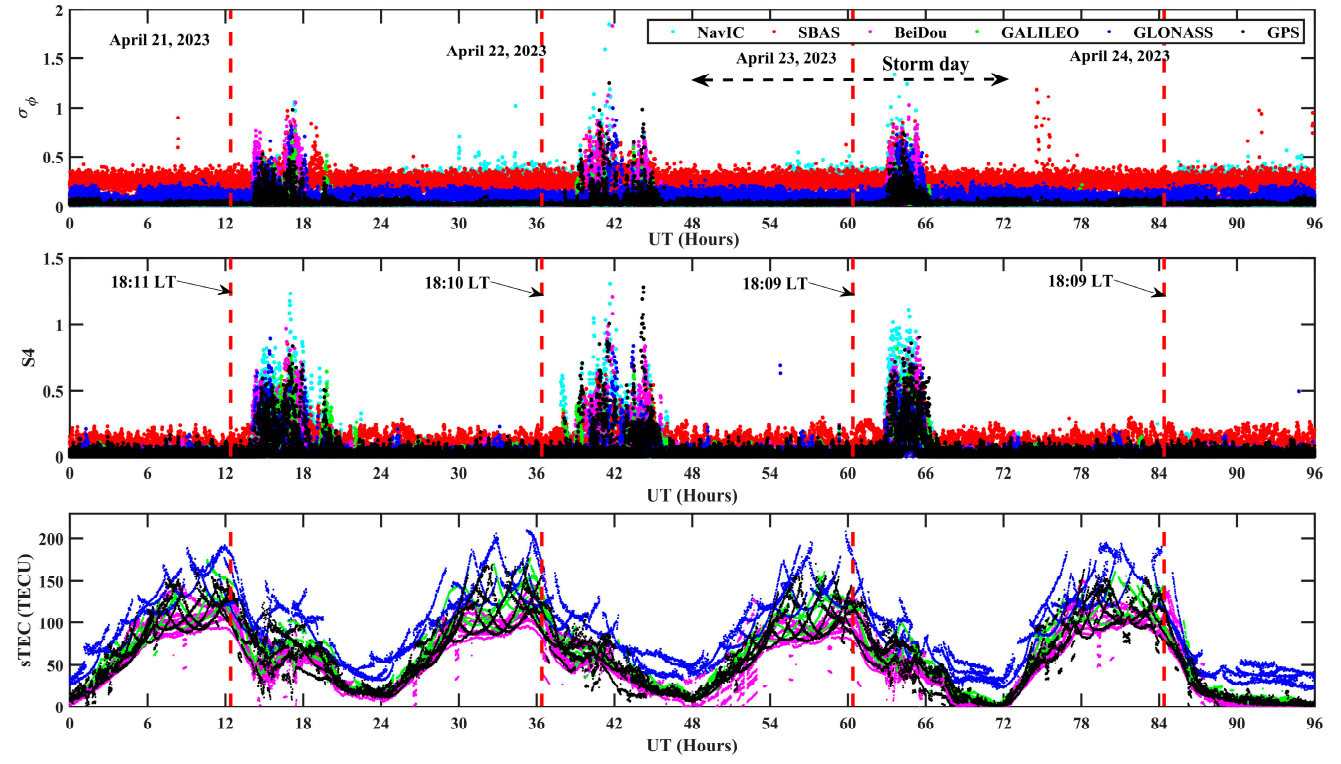

Figure 6. The σ_φ (**top panel**), S4 (**middle panel**) and sTEC (**bottom panel**) from all the available constellations on the days before the storm (21, 22 April), during the storm (23 April), and after the storm (24 April) in 2023. The red dashed line shows the local sunset terminator for the above days.

To identify the PRNs affected by significant depletions and thereby meet the criteria for their association with EPBs, we concentrate on the regular occurrence duration of EPBs (15:00 UT to 18:00 UT) for all storm events. From Figure 7, it can be seen that the TEC depletions (red color) meet the plasma bubble criteria only on 23 April 2023. On the other hand, the rest of the geomagnetic storm events (27 February, 24 March) hardly evidence any noticeable TEC depletion (grey color), inferring that the regular post-sunset EPBs were suppressed during these periods owing to the disagreement of electrodynamics for manifesting a PRE at the evening terminator. The TEC value is additionally reduced by processes such as the rapid nighttime recombination of the F-layer followed by density re-distribution. These two processes result in shallow TEC slopes and lack the recovery section; however, they both were removed from our TEC depletion statistics as they do not satisfy the association criteria for the presence of EPBs. Although there are TEC depletions (blue color) observed on 23 March 2023, they hardly meet the thresholds set for EPBs and may rather incur noises due to gravity waves, neutral wind shear, medium-scale travel ionospheric disturbances (MSTIDs), etc.

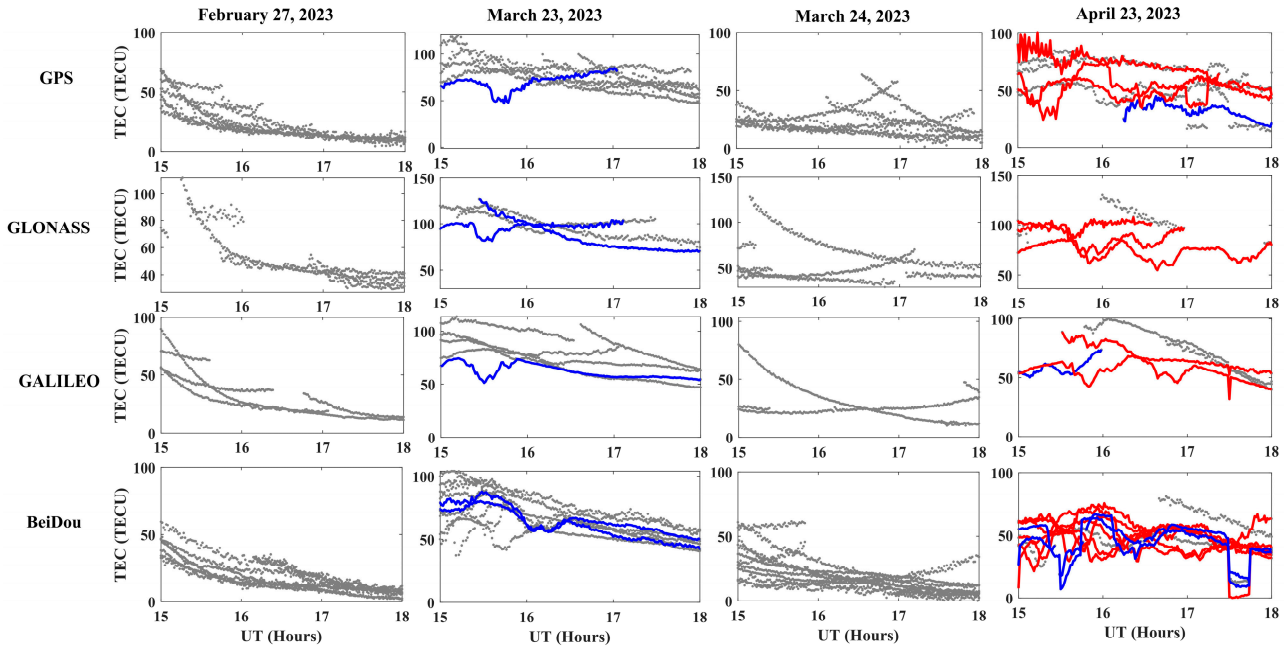

Figure 7. The observed sTEC for all the available GNSS constellations (GPS, GLONASS, Galileo, BeiDou) with depletion depths Δ(sTEC) < 5 TECU (grey), 5 ≤ Δ(sTEC) < 10 TECU (blue), and Δ(sTEC) ≥ 10 TECU (red) during the four geomagnetic storm days considered in this study.

Figure 8 depicts the ionospheric piercing points (IPP) at each time of the observed satellites above the receiver location during the geomagnetic storm event on 23 April 2023 determining the localization characteristics of EPBs corresponding to GNSS-observed scintillation indices. The color bar in each plot (left and right) indicates the intensities for the S4 and σ_{φ}, respectively. The shaded points represent the IPP positions with no significant scintillation intensity. The red and green line shows the location of the magnetic equator and the approximate equatorial ionization crest anomaly (EIA) location. We note that lower threshold limits are considered for the respective S4 and σ_{φ} index plots to eliminate the presence of noises which are irreverent to the scintillation phenomena. In Figure 9, we analyze the ROTI variation on 23 April 2023 geomagnetic storm day at the present location (KLEF) and that obtained from SIMuRG for other geodetic GNSS stations under the IGS network (IISC, HYDE, and LCK3), ranging from near equatorial latitude to outer edge of equatorial ionization anomaly (EIA) crest latitude. The results confirm the prevailing TEC irregularities confined to the EIA region, substantiating the connection between TEC depletion at the location and prevailing EPBs over the Indian longitude sector.

The results are in good agreement with the earlier review of EPBs in the global equatorial and low-latitude region indicating the latitudinal extent of bubbles of approximately ±15° geomagnetic latitudes [7].

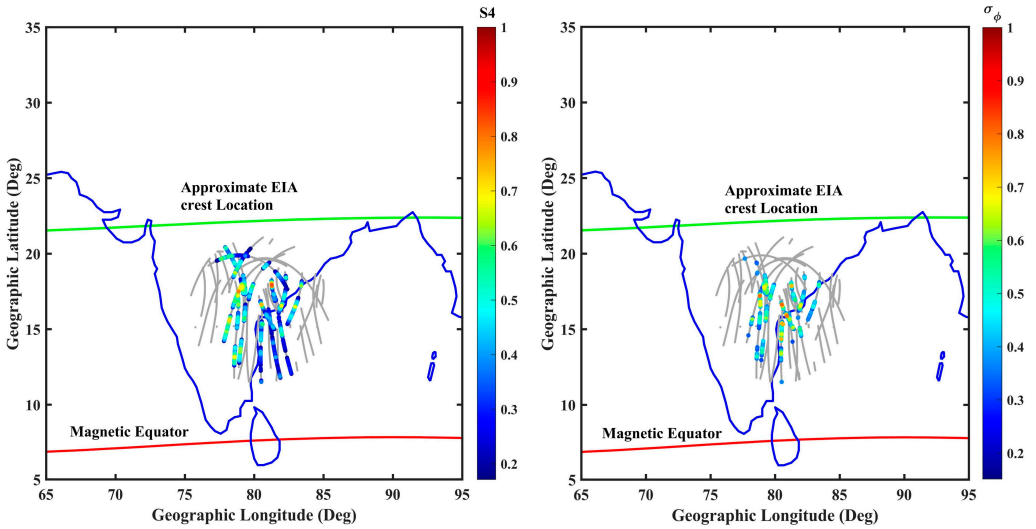

Figure 8. Geographic map of India showing the location of the GISTM receiver and EPBs overhead from the recorded scatter points of S4 (**left**) and σφ (**right**) indices at ionospheric piercing points (IPPs; gray color). The color bars indicate the level of the scintillation indices. The approximate locations of magnetic equator and EIA crest are shown in red and green color contours, respectively.

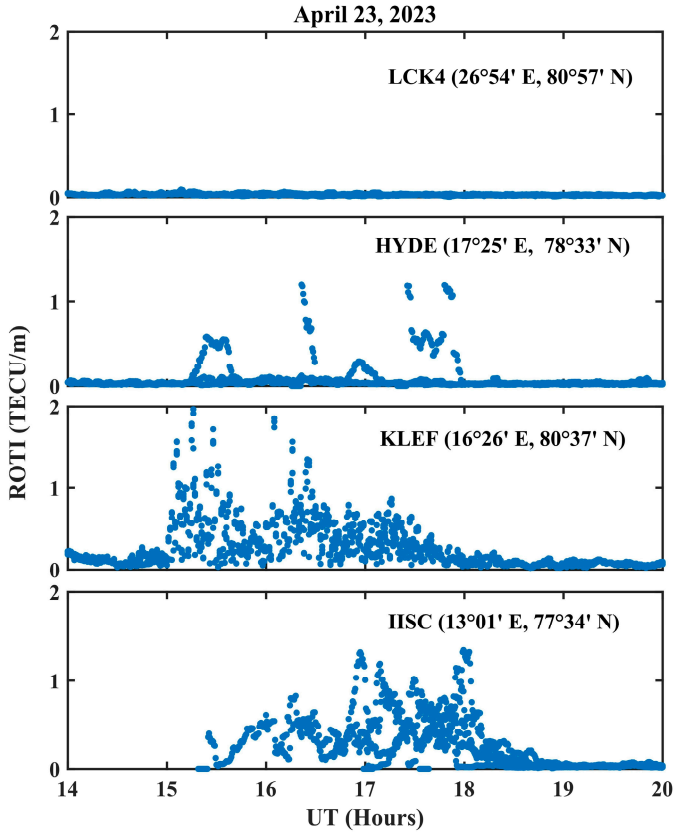

Figure 9. ROTI variation at the present location (KLEF) and other geodetic GNSS stations under IGS network (IISC, HYDE, and LCK3), ranging from near equatorial latitude to outer edge of equatorial ionization anomaly (EIA) crest latitude in the Indian longitude sector on 23 April 2023, a geomagnetic storm day.

Figure 10 depicts the TEC (black) retrieved from PRNs 2, 10, 18 and 32 belonging to the GPS constellation and the respective scintillation indices (S4 in blue and σ_φ in orange) for Signal 1 (refer to Table 1) along with the elevation angles (pink) on 23 April 2023. The possible association of EPBs can be inferred from the significant TEC depletions in the signals from selected PRNs. We note that the TEC depletion time and the scintillation activity are between 15:00 UT and 18:00 UT. In all the above PRNs, the minimum in the TEC depletion curve synchronizes with the maximum value of scintillation indices (S4 and σ_φ). All the depletions in the TEC detrended curve satisfy the plasma bubble criteria in terms of depletion depth (10 to 45 TECU), apparent duration (10 to 45 min), and maximum values (12.6 to 18.5 TECU) around the depletion. When an anomaly is observed in multiple station satellite pairs, the anomaly is due to the real ionospheric effect and not due to the receiver bias or data error. To further emphasize the association of EPBs, we analyze TEC depletions from other available GNSS constellations like GLONASS, Galileo, and BeiDou as multi-GNSS measurements could contribute to increasing the spatial coverage of the ionosphere and better understanding the local morphology of its fluctuations [86].

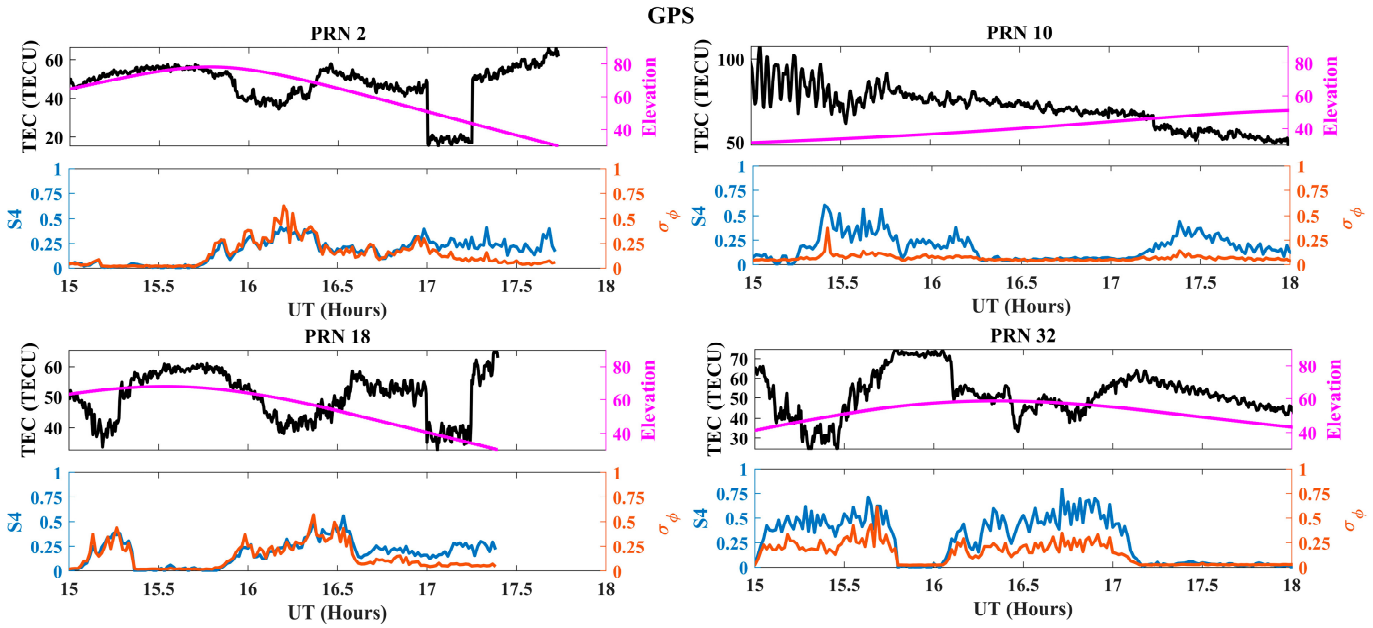

Figure 10. The sTEC (black), elevation angle (pink) and their respective scintillation indices S4 (blue) and σ_φ (orange) of the GPS PRNs 2, 10, 18 and 32, confirming depleted TEC between 15:00 UT and 18:00 UT on the 23 April 2023 geomagnetic storm day.

In Figure 11, we show the TEC (black) with elevation angle (pink), S4 (blue) and σ_φ (orange) of Signal 1 for PRNs 44, 58 and 59 under the GLONASS constellation. PRN 59 seems to be indicating the presence of EPB for a longer period than the other two PRNs as it is showing multiple depletion depths. All the depletions in the span of 15:00 UT to 18:00 UT satisfy the plasma bubble criteria and agree well with the S4 and σ_φ variations. Figure 12 depicts the TEC (black), elevation angle (pink), S4 (blue) and σ_φ (orange) of Signal 1 for the PRNs affected by the plasma bubble in the Galileo constellation. Only two PRNs (82 and 89) are affected by the plasma bubble. The depletion in PRN 89 is higher than in PRN 82 and the elevation angle is >40°. Figure 13 projects the TEC (black) with elevation angle (pink), S4 (blue) and σ_φ (orange) of Signal 1 for the PRNs affected in the BeiDou constellation due to EPBs. A good number of satellites (PRN 142, 148, 149, 152, 153, and 156) from this constellation witness depletions fulfilling the criteria for possible association of EPBs. In the BeiDou constellation, more than two depletion depths are observed in all the PRNs showing the sensitivity of the constellation to the EPBs which are verified to match well with the collocated scintillation indices (S4 and σ_φ). Hence, from Figures 10–13, it is

evident that in all the constellations, the observed PRNs are encountered with depletions in TEC for a short period within the span of 15:00 UT to 18:00 UT (20:30 LT to 23:30 LT) that falls in the local post-sunset hours to midnight. The results are in good agreement with the earlier studies [38,39,87]. It is important to mention that an elevation angle threshold (>30°) is applied throughout the study irrespective of PRNs to avoid contaminations with possible multipath and ground interference errors. The S4 and σ_φ indices recorded by the receiver are also seen to be ranging from moderate to high-intensity levels, whose peaks follow the TEC depletion characteristic curves, suggesting a close relationship between the depletion and scintillation indices under the influence of EPBs.

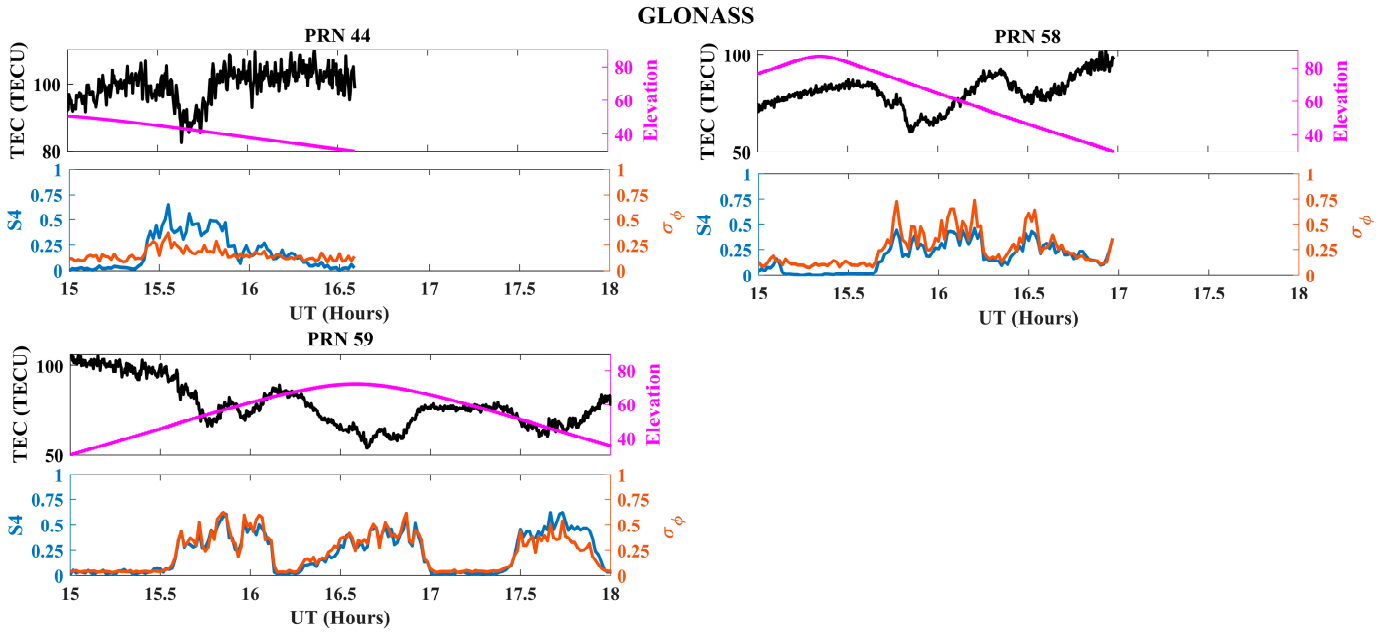

Figure 11. The sTEC (black), elevation angle (pink) and their respective signal 1 scintillation indices S4 (blue) and σ_φ (orange) of the GLONASS PRNs 44, 58 and 59, showing the depleted TEC between 15:00 UT to 18:00 UT on the 23 April 2023 geomagnetic storm day.

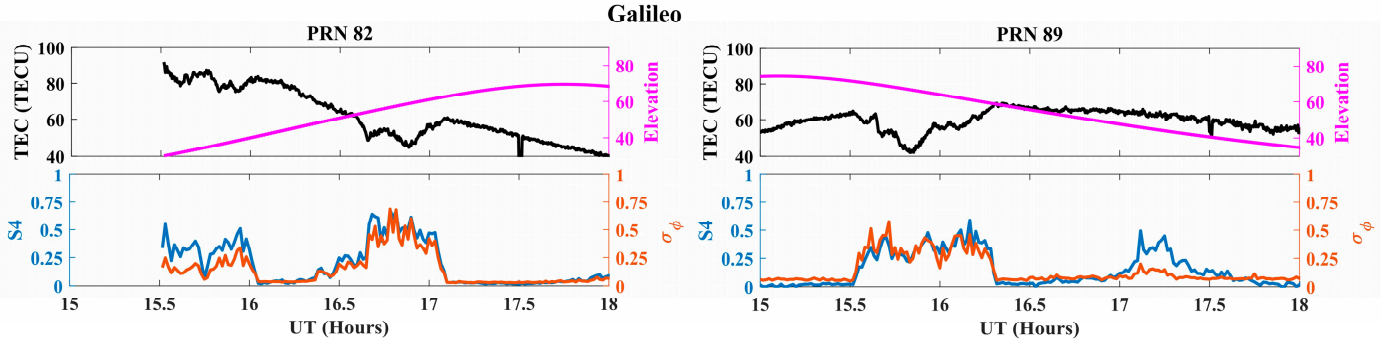

Figure 12. The sTEC (black), elevation angle (pink) and their respective Signal 1 scintillation indices S4 (blue) and σ_φ (orange) of the Galileo PRNs 82 and 89, showing depleted TEC between 15:00 UT and 18:00 UT on the 23 April 2023 geomagnetic storm day.

The maximum Δ(sTEC), t_{sTEC}, and the corresponding delays of available frequencies in the respective constellations are given in Table 3. The GPS shows the highest depletion depth of ~45 TECU within the maximum apparent duration of 48 min. The Galileo and GLONASS also show extended duration but with lesser depletion depths, suggesting that there may be less impact of EPBs on these constellations. The GPS exhibits a high ionospheric delay of 7.29 m in their L1 frequency followed by the GAGAN with a delay of

6.8 m in L1. BeiDou shows the least ionospheric delay in B1 (5.28 m) and the highest in B2 (8.83 m), unlike the GPS which exhibited the lowest in L1 (7.29 m) and the highest in L3 (13.09 m). Galileo shows the lowest ionospheric delay of 3.56 m out of all the constellations.

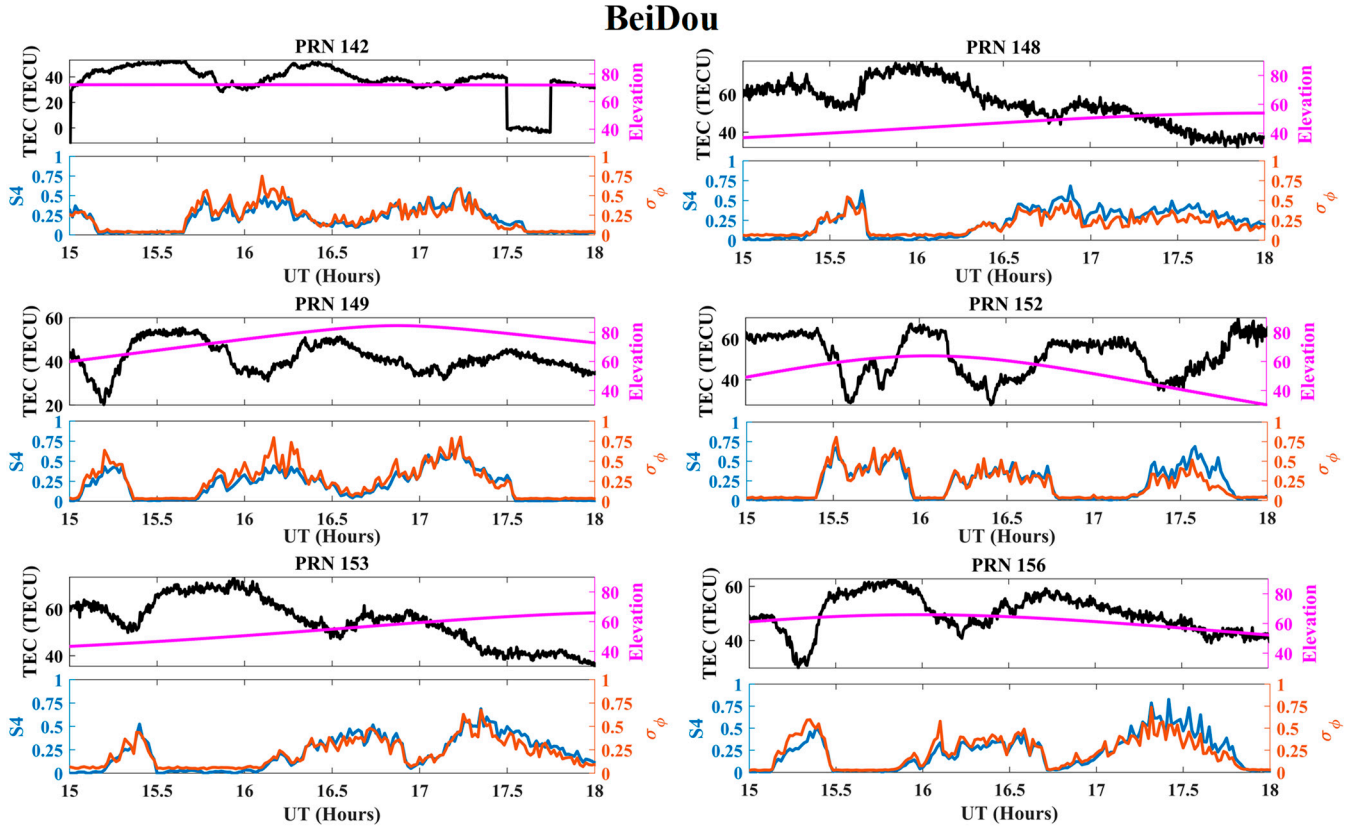

Figure 13. The sTEC (black), elevation angle (pink) and their respective Signal 1 scintillation indices S4 (blue) and σ_φ (orange) of the BeiDou PRNs 142, 148, 149, 152, 153, and 156, showing the depleted TEC between 15:00 UT and 18:00 UT on the 23 April 2023 geomagnetic storm day.

Table 3. The maximum sTEC depletion depth Δ(sTEC), apparent duration t_{sTEC}, and their corresponding ionospheric delay for all the GNSS constellations and their available frequencies.

S. No	GNSS Constellation	Maximum Depletion Depth Δ(sTEC) in TECU	Apparent Duration (t_{sTEC}) in Minutes	Ionospheric Delays in Meters		
				Signal 1	Signal 2	Signal 3
1	GPS (G)	45	48	7.29	12.05	13.09
2	GLONASS (R)	25	45	3.92	6.47	-
3	Galileo (E)	22	40	3.56	5.87	6.40
4	BeiDou (C)	32	28	5.28	8	8.83
5	GAGAN (S)	NA	NA	NA	NA	NA
6	IRNSS/NavIC (I)	NA	NA	NA	NA	NA

Here, NA implies not applicable, the GAGAN TEC is not included as the biases are not being corrected in the present receiver, whereas NavIC TEC is not recorded by the receiver as only one signal (L5) is tracked at present.

To further understand the severity of scintillation activity, we classify S4 and σ_φ into weak ($0.17 \leq S4 < 0.3$; $0.15 \leq \sigma_\varphi < 0.5$), moderate ($0.3 \leq S4 \leq 0.5$; $0.5 \leq \sigma_\varphi \leq 0.8$), and strong ($S4 > 0.5$; $\sigma_\varphi > 0.8$) following the acceptable limits [88,89]. Figure 14 shows a clear enhancement of scintillation indices (S4 in blue and σ_φ in orange) from 15:00 UT to 18:00 UT in Signal 1 under GAGAN (PRNs 127, 128, and 132). We note that all the above PRNs are geostationary satellites (GEOs) having a fixed elevation and azimuth from the location of observation. Further, scintillation indices S4 (blue) and σ_φ (orange) for Signal 2 are given

in Figure 15a for GPS, GLONASS, and Galileo and in Figure 15b for BeiDou constellations. It is important to mention that GAGAN does not have any frequency matching with Signal 2, whereas the NavIC system does not carry legacy Signals 1 and 2 as per the categories of signals listed in Table 1. The high intensities of the S4 and σ_φ coincide with the depletion depth. While the GPS constellation has the maximum S4 values compared to all the other constellations, BeiDou shows the maximum level of σ_φ among all constellations. In Figure 16a,b, we present S4 and σ_φ variations for Signal 3 under global (GPS, Galileo, and BeiDou) and Indian (GAGAN and NavIC) constellations. However, we cannot present the corresponding scintillation indices for GLONASS as it does not include Signal 3 at present in the ISMR recordings. Figures 15b and 16a show frequent enhancement of scintillation indices corresponding to signals under the BeiDou constellation, demonstrating relatively longer effects of EPBs. The scintillation values in all the PRNs in Figures 13–16 lie within moderate to strong scintillation activity as per the classification scheme for S4 and σ_φ followed in our study. A quick overview of the maximum levels of S4 and σ_φ in all the GNSS constellations and their respective frequencies can be obtained from Table 4. It is also clear from S4 and σ_φ variability that the level of the scintillation effect is inversely proportional to the signal frequency demonstrating relative dependance of scintillation effects on the penetrating power of the signals. The results reported are consistent with the previous studies showing the scintillations associated with EPBs during the post-sunset hours and their decaying after the midnight period [14,39,76]. Moreover, the impact of the depleted TEC during scintillation activity is realized in terms of ionospheric delays that are supported by enhanced S4, σ_φ, and ROTI indices in our study.

Table 4. The maximum scintillation indices (S4 and σ_φ) of the available frequencies in the GNSS constellations on the 23 April 2023 geomagnetic storm day.

S.No	GNSS Constellation	Signal 1		Signal 2		Signal 3	
		Max S4	Max σ_φ	Max S4	Max σ_φ	Max S4	Max σ_φ
1	GPS (G)	0.79	0.61	1.00	0.64	1.09	0.69
2	GLONASS (R)	0.45	0.73	0.70	0.90	NA	NA
3	Galileo (E)	0.58	0.57	0.90	0.73	0.86	0.72
4	BeiDou (C)	0.68	0.80	0.99	0.99	0.92	0.86
5	GAGAN (S)	0.62	0.75	NaN	NaN	0.94	0.93
6	IRNSS/NavIC (I)	NA	NA	NA	NA	0.97	0.98

Here, NA implies not applicable as the corresponding parameters are not available in the respective constellations recorded by the receiver.

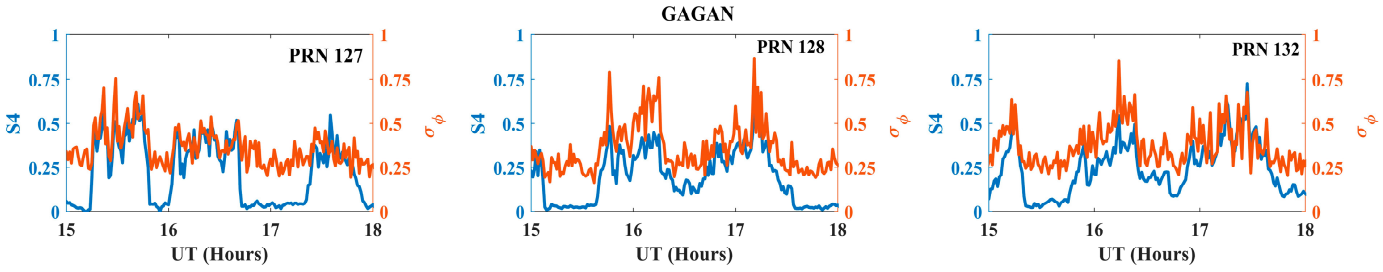

Figure 14. The S4 (blue) and σ_φ (orange) of Signal 1 for all the affected PRNs in the GAGAN constellations between 15:00 UT and 18:00 UT on the 23 April 2023 geomagnetic storm day.

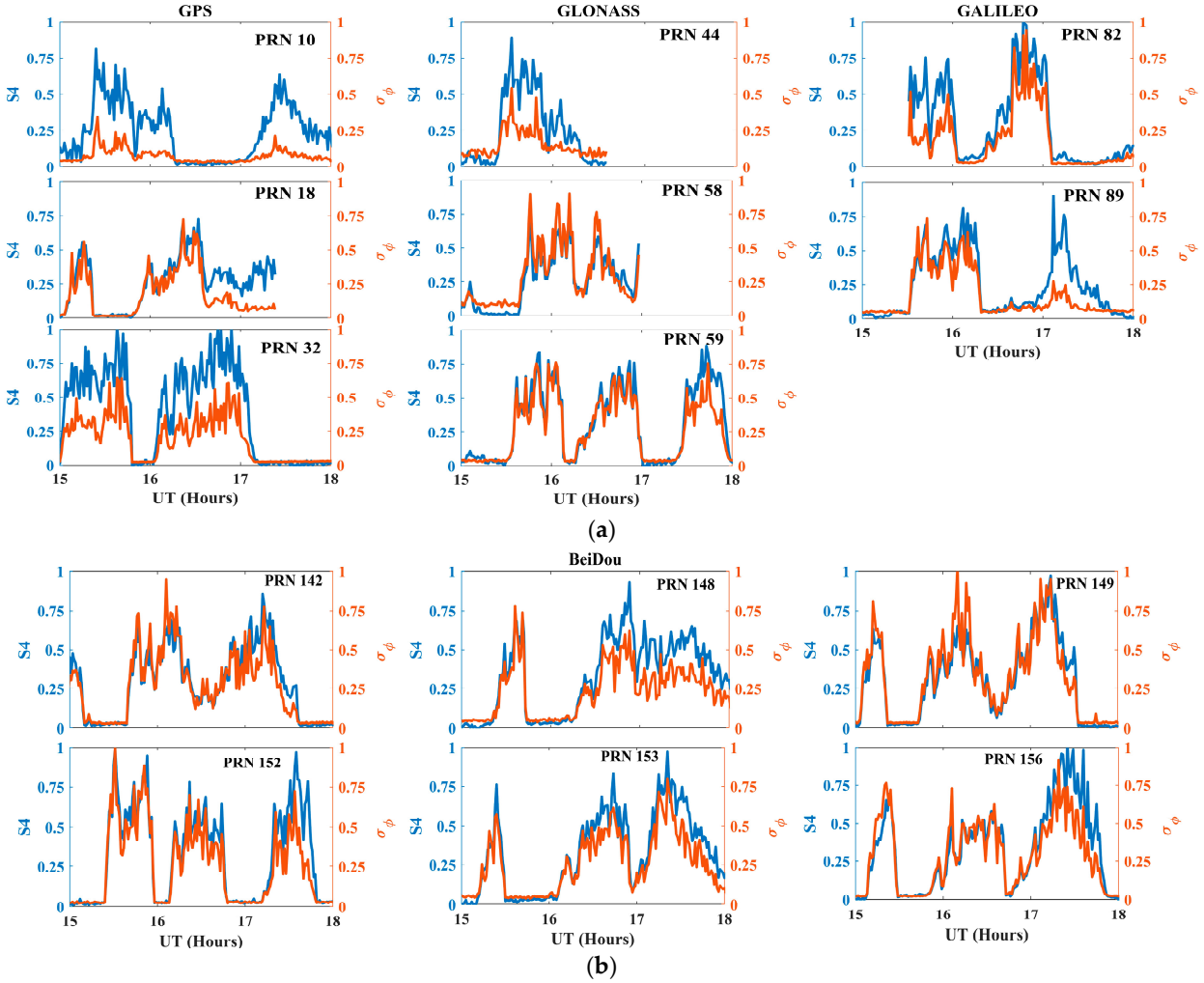

Figure 15. (**a**) The S4 (blue) and σ_φ (orange) of Signal 2 for all the available PRNs, showing the TEC depletions in the GPS, GLONASS and Galileo constellations between 15:00 UT and 18:00 UT on the 23 April 2023 geomagnetic storm day. (**b**) The S4 (blue) and σ_φ (orange) of Signal 2 for all the available PRNs showing the TEC depletions in the BeiDou constellation.

Concerning the association of TEC depletions and scintillation activity with the occurrence of EPBs at the present low-latitude location, the EPBs are considered to be the depleted plasma density regions typically seen under the influence of the equatorial electrodynamics. In the present work, we determine the TEC depletion characteristics by detrending the high-resolution (15 s) sTEC observables from signals under different GNSS constellations at a low-latitude location with a 60 min window size during the geomagnetically disturbed days. Threshold constraints like depletion depth (10 TECU) and depletion duration (10 to 180 min) are applied to selectively choose the sTEC depletions that highly correspond to the EPB occurrences over the region. Magdaleno et al. [90] employed a moving average window of 10 min to extract the depletions associated with EPBs by a depletion depth threshold of 5 TECU. Similarly, Mersha et al. [38] used a 60 min window size to calculate the moving average and obtained the detrended TEC to find out the possible occurrence of the plasma bubble with a minimum depletion depth of 10 TECU. A similar method was applied by Portillo et al. [14] with a 91 min window size and 10 TECU depletion depth threshold for a 10 min resolution sTEC data to find the plasma bubble activity in the African region. However, the earlier literature and the observations from the present work demonstrate that a 60 min window size with a depletion depth of 10 TECU is the best combination of thresholds to suitably identify the depletions highly associated with EPBs. Thus, the present method of indirectly detecting the presence of EPBs could disregard TEC

depletions due to the travel ionospheric disturbances, F-layer disturbances, and reduced density owing to the spread of ions by the Fountain effect.

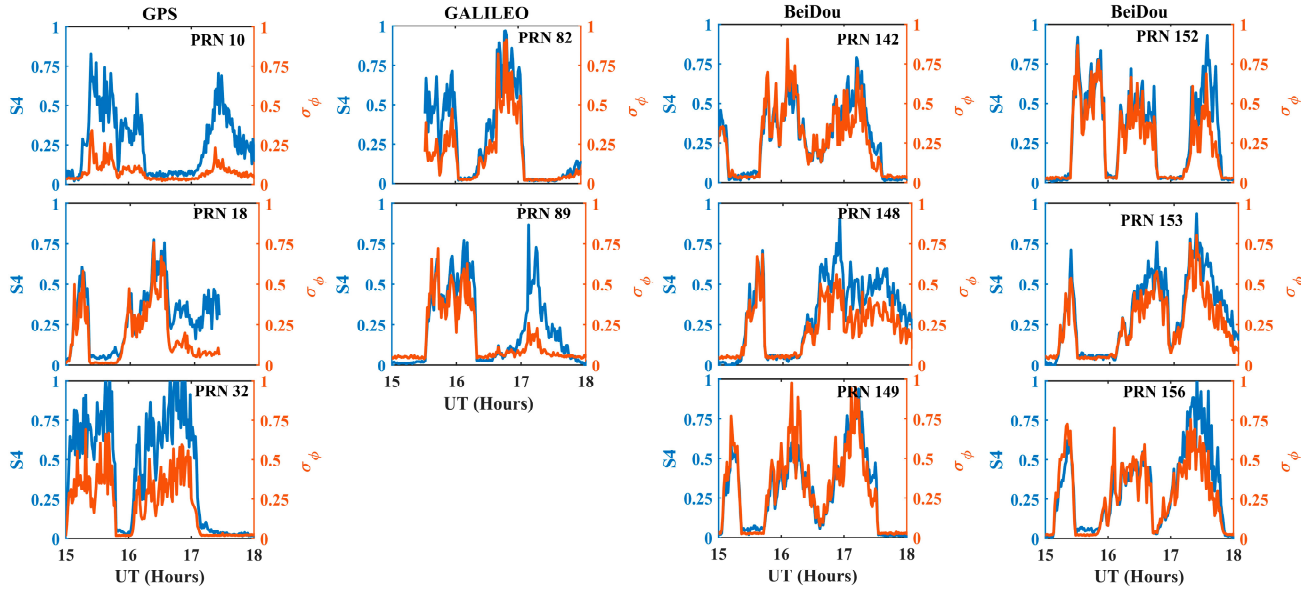

(**a**)

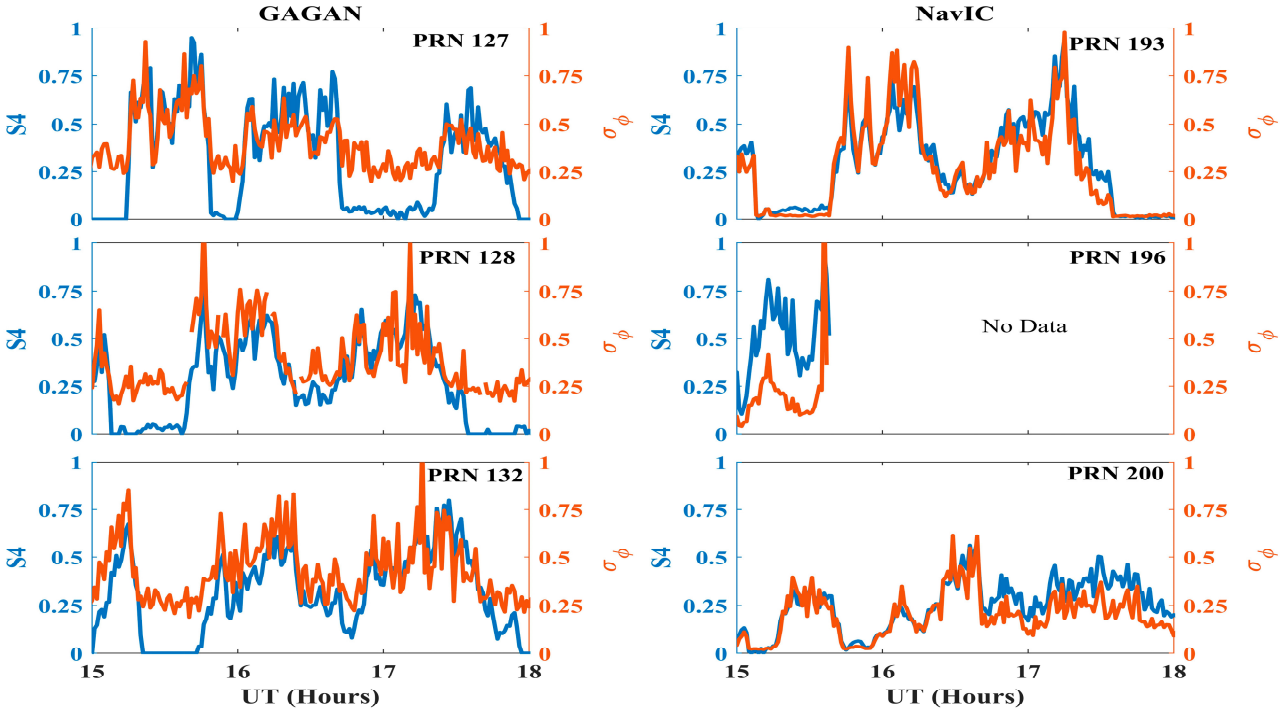

(**b**)

Figure 16. (**a**) The S4 (blue) and σ_φ (orange) of Signal 3 for all the available PRNs showing the TEC depletions in the GPS, Galileo, and BeiDou constellations between 15:00 UT and 18:00 UT on the 23 April 2023 geomagnetic storm day. (**b**) The PRNs of the GAGAN and NavIC in constellation having severe scintillations (S4 (blue) and σ_φ (orange)) between 15:00 UT and 18:00 UT on the 23 April 2023 geomagnetic storm day.

Moreover, attributing the TEC depletion characteristics to the prevailing EPBs is supported by a strong agreement with the high-intensity scintillation indices in our study. It is important to mention that the shallow sTEC depletions correspond to the weak or no-scintillation intensity in all the above PRNs and constellations, emphasizing the weakening of the EPB after the local midnight periods that is in agreement with the

previous studies [91]. The upward E × B drift is a crucial factor in the investigation of ionospheric scintillations because it triggers plasma density anomalies, which produce greater scintillations at far low-latitude locations than at the magnetic equator [9]. The present study at a low-latitude location enabled us to emphasize the strong relationship of the TEC depletion and scintillation indices which are altogether associated with the EPBs and are responsible for degrading the performances or even causing loss of locks in satellite-based services.

4. Summary and Conclusions

In this study, the sTEC depletion characteristics are investigated during the geomagnetic storm days (Dst < −100 nT) in the ascending phase of Solar cycle 25 to ascertain possible triggering or suppression of the EPBs. Following the criterion for detecting the presence of EPBs from the corresponding sTEC depletion characteristics, such as depletion depth Δ(sTEC), apparent duration (t_{sTEC}), and maximum values around the depletion, we confirm that out of the three storm events considered in this study, only one event (23 April 2023) is associated with an enhanced EPBs, whereas, during the rest of the events, the regular EPBs are notably suppressed. The storm events on 27 February as well as 23 and 24 March in 2023 report inhibited TEC depletion, confirming suppressed EPBs during the period that is supported by subdued S4 (0 to 0.48) and σ_{φ} (0.01 to 0.59) indices. However, the observations on 23 April 2023 confirm that all GNSS constellations witness sTEC depletions between 15:00 UT and 18:00 UT, which is in good agreement with the recorded scintillation indices (S4 and σ_{φ}). The ROTI variations at locations ranging from near equatorial latitude to the outer edge of the EIA crest latitudes in the same longitude sector corroborate the prevailing irregularities due to EPBs above the region. In brief, the characteristic depletion depths (22 to 45 TECU) and depletion times (28 to 48 min) across different constellations confirm the triggering of EPBs during the geomagnetic storm event on 23 April 2023. We argue the possible enhanced dusk time pre-reversal enhancement (PRE) is the cause for the instability observed in the sTEC magnitudes.

Moreover, 23 April 2023 witnessed moderate-to-strong scintillations across signals from all constellations as per the classification scheme based on the scintillation indices. The signals from GPS show the largest depletion of ~48 TECU within an apparent duration of 45 min, whereas that of Galileo present the least depletion depth of ~22 TECU with an apparent duration of 40 min. Although the signals from the BeiDou constellation have the smallest duration of 22 min, they evidence repeated depletions during the observed span, confirming relatively more vulnerability to the storm onset. We perform an analysis of the equivalent ionospheric delay to realize the consequences of TEC depletions in respective frequencies of the GNSS constellations that confirms the maximum delay (~13.09 m) in GPS L5, whereas the minimum delay (3.56 m) is seen in Galileo L1. Similarly, the maximum S4 is observed in the GPS constellation, while the largest σ_{φ} is observed in the BeiDou constellation in all three frequencies.

In brief, the present objective attempts to strengthen the relation between sTEC depletion and scintillation indices observed through a high-rate GISTM receiver; both effects are the consequences of the development of EPBs at the equatorial and low-latitude regions. The future assignment of this work is to include a greater number of geomagnetic storms as they occur for substantiating the hypothesis adopted in this study. An established relationship between TEC depletion and EPBs could pave the way for employing the most abundant traditional geodetic GNSS receivers established under IGS and UNAVCO along with other regional and individual stations to participate in understanding and modeling the sTEC depletions associated with EPBs and developing regional as well as global scintillation mitigation strategies. In addition, the opportunity of multi-constellation signal availability opens a doorway for maneuvering the adaptation of interoperability among signals to enhance the performance of satellite-based navigation, positioning and timing solutions under intense ionospheric scintillations. The supporting method trailing the presence of EPBs through TEC depletion threshold criteria used in this study opens the

scope for utilizing non-scintillation geodetic GNSS receiver observations as the abundance of scintillation monitoring receivers, ionosonde, radar, and other observatories are sparse across any region compared to the spread of geodetic GNSS observatories. Nevertheless, the study foresees scopes for a better understanding of the effects of plasma irregularities (scintillations, fading and depletions) on GNSS signals due to the occurrence of EPBs and developing their mitigation techniques through improved modeling and forecasting services. Our attempts at such objectives coincide with the global efforts for mitigating scintillation effects in satellite-based critical and dynamic services and applications.

Author Contributions: Conceptualization, S.K.P. and P.J.; methodology, S.K.P., P.J. and R.K.V.; software M.I.H.S., G.K.S. and R.K.V.; validation, P.J., G.K.S., M.I.H.S. and S.K.P.; formal analysis, P.J., G.K.S., S.K.P. and R.K.V.; investigation, P.J., S.K.P. and R.K.V.; resources, G.K.S. and S.K.P.; data curation, S.K.P.; writing—original draft preparation, R.K.V. and S.K.P.; writing—review and editing, R.K.V., P.J., G.K.S., M.I.H.S. and S.K.P.; visualization, P.J., G.K.S., M.I.H.S. and S.K.P.; supervision, S.K.P.; project administration, S.K.P.; funding acquisition, P.J., M.I.H.S. and S.K.P. All authors have read and agreed to the published version of the manuscript.

Funding: SKP and RKV appreciate the Core Research Grant (CRG) project sponsored by the Science Engineering Research Board (SERB) (A statutory body of the Department of Science and Technology, Government of India) New Delhi, India, vide File No: CRG/2019/003394. PJ acknowledges the financial support for this research from Fundamental Fund (FF67) of the Thailand Science Research and Innovation Fund (Annual Budget B.E. 2567). MIHS extend the appreciation to the Researchers Supporting Project number (RSPD2023R999), King Saud University, Riyadh, Saudi Arabia.

Data Availability Statement: The Disturbance storm index (Dst), geomagnetic Kp index, ap index, and interplanetary magnetic field component (IMF-Bz) data are downloaded from the NASA-OMNI website (https://omniweb.gsfc.nasa.gov/ (accessed on 5 August 2023)). The multi-constellation and multi-frequency GNSS sTEC data are obtained from the Septentrio PolaRx5S GNSS receiver established at the study location. The TEC validation is performed with the additional TEC retrieving software TayAbsTEC (http://www.gnss-lab.org/tay-abs-tec.html (accessed on 3 October 2023)) and GPS-TEC analysis (https://seemala.blogspot.com/2020/12/gps-tec-program-version-3-for-rinex-3.html (accessed on 3 October 2023)), obtained from their respective website. The ROTI data for the IGS stations over Indian region is obtained from the SIMuRG: System for Ionosphere Monitoring and Research from GNSS website (https://simurg.space/ (accessed on 3 October 2023)).

Acknowledgments: SKP and RKV acknowledge Koneru Lakshmaiah Education Foundation for providing laboratory and infrastructure for establishment of GISTM receiver and conducting the present research. "MIHS extends the appreciation to the Researchers Supporting Project number (RSPD2023R999), King Saud University, Riyadh, Saudi Arabia" for providing funds to conduct the present research at the present university.

Conflicts of Interest: The authors declare no conflict of interest. The funders had no role in the design of the study; in the collection, analyses, or interpretation of data; in the writing of the manuscript, or in the decision to publish the results.

References

1. Gentile, L.C.; Burke, W.J.; Rich, F.J. A Global Climatology for Equatorial Plasma Bubbles in the Topside Ionosphere. *Ann. Geophys.* **2006**, *24*, 163–172. [CrossRef]
2. Katamzi-Joseph, Z.T.; Habarulema, J.B.; Hernández-Pajares, M. Midlatitude Postsunset Plasma Bubbles Observed over Europe during Intense Storms in April 2000 and 2001. *Space Weather* **2017**, *15*, 1177–1190. [CrossRef]
3. Kumar, S. Morphology of Equatorial Plasma Bubbles during Low and High Solar Activity Years over Indian Sector. *Astrophys. Space Sci.* **2017**, *362*, 93. [CrossRef]
4. Xiong, C.; Stolle, C.; Lühr, H.; Park, J.; Fejer, B.G.; Kervalishvili, G.N. Scale Analysis of Equatorial Plasma Irregularities Derived from Swarm Constellation. *Earth Planets Space* **2016**, *68*, 121. [CrossRef]
5. Patil, A.S.; Nade, D.P.; Taori, A.; Pawar, R.P.; Pawar, S.M.; Nikte, S.S.; Pawar, S.D. A Brief Review of Equatorial Plasma Bubbles. *Space Sci. Rev.* **2023**, *219*, 16. [CrossRef]
6. Lühr, H.; Xiong, C.; Park, J.; Rauberg, J. Systematic Study of Intermediate-Scale Structures of Equatorial Plasma Irregularities in the Ionosphere Based on CHAMP Observations. *Front. Phys.* **2014**, *2*, 15.
7. Bhattacharyya, A. Equatorial Plasma Bubbles: A Review. *Atmosphere* **2022**, *13*, 1637. [CrossRef]

8. Seemala, G.K.; Valladares, C.E. Statistics of Total Electron Content Depletions Observed over the South American Continent for the Year 2008. *Radio Sci.* **2011**, *46*, 1–14. [CrossRef]
9. Ndinya, B.; George, O.; Uluma, E. Occurrence Characteristics of Equatorial Plasma Bubbles over Kisumu, Kenya during Solar Maximum of Solar Cycle 24. *Int. J. Adv. Astron.* **2021**, *9*, 1–9. [CrossRef]
10. Patra, A.K.; Taori, A.; Chaitanya, P.P.; Sripathi, S. Direct Detection of Wavelike Spatial Structure at the Bottom of the F Region and Its Role on the Formation of Equatorial Plasma Bubble. *J. Geophys. Res. Space Phys.* **2013**, *118*, 1196–1202. [CrossRef]
11. Li, G.; Ning, B.; Abdu, M.A.; Wan, W.; Hu, L. Precursor Signatures and Evolution of Post-Sunset Equatorial Spread-F Observed over Sanya. *J. Geophys. Res. Space Phys.* **2012**, *117*, A08321. [CrossRef]
12. Ott, E. Theory of Rayleigh-Taylor Bubbles in the Equatorial Ionosphere. *J. Geophys. Res. Space Phys.* **1978**, *83*, 2066–2070. [CrossRef]
13. Magdaleno, S.; Cueto, M.; Herraiz, M.; Rodríguez-Caderot, G.; Sardón, E.; Rodríguez, I. Ionospheric Bubbles Detection Algorithms: Analysis in Low Latitudes. *J. Atmos. Sol.-Terr. Phys.* **2013**, *95–96*, 65–77. [CrossRef]
14. Portillo, A.; Herraiz, M.; Radicella, S.M.; Ciraolo, L. Equatorial Plasma Bubbles Studied Using African Slant Total Electron Content Observations. *J. Atmos. Sol.-Terr. Phys.* **2008**, *70*, 907–917. [CrossRef]
15. Kriegel, M.; Jakowski, N.; Berdermann, J.; Sato, H.; Mersha, M.W. Scintillation Measurements at Bahir Dar during the High Solar Activity Phase of Solar Cycle 24. *Ann. Geophys.* **2017**, *35*, 97–106. [CrossRef]
16. Kintner, P.M.; Ledvina, B.M.; de Paula, E.R. GPS and Ionospheric Scintillations. *Space Weather* **2007**, *5*, S09003. [CrossRef]
17. Demyanov, V.V.; Yasyukevich, Y.V. Space Weather: Risk Factors for Global Navigation Satellite Systems. *Solnechno-Zemn. Fiz.* **2021**, *7*, 30–52. [CrossRef]
18. Pradipta, R.; Doherty, P.H. Assessing the Occurrence Pattern of Large Ionospheric TEC Gradients over the Brazilian Airspace. *NAVIGATION* **2016**, *63*, 335–343. [CrossRef]
19. Li, Q.; Zhu, Y.; Fang, K.; Fang, J. Statistical Study of the Seasonal Variations in TEC Depletion and the ROTI during 2013–2019 over Hong Kong. *Sensors* **2020**, *20*, 6200. [CrossRef]
20. De Michelis, P.; Consolini, G.; Pignalberi, A.; Lovati, G.; Pezzopane, M.; Tozzi, R.; Giannattasio, F.; Coco, I.; Marcucci, M.F. Ionospheric Turbulence: A Challenge for GPS Loss of Lock Understanding. *Space Weather* **2022**, *20*, e2022SW003129. [CrossRef]
21. De Michelis, P.; Consolini, G.; Tozzi, R.; Pignalberi, A.; Pezzopane, M.; Coco, I.; Giannattasio, F.; Marcucci, M.F. Ionospheric Turbulence and the Equatorial Plasma Density Irregularities: Scaling Features and RODI. *Remote Sens.* **2021**, *13*, 759. [CrossRef]
22. De Michelis, P.; Consolini, G.; Alberti, T.; Tozzi, R.; Giannattasio, F.; Coco, I.; Pezzopane, M.; Pignalberi, A. Magnetic Field and Electron Density Scaling Properties in the Equatorial Plasma Bubbles. *Remote Sens.* **2022**, *14*, 918. [CrossRef]
23. Pezzopane, M.; Pignalberi, A.; Coco, I.; Consolini, G.; De Michelis, P.; Giannattasio, F.; Marcucci, M.F.; Tozzi, R. Occurrence of GPS Loss of Lock Based on a Swarm Half-Solar Cycle Dataset and Its Relation to the Background Ionosphere. *Remote Sens.* **2021**, *13*, 2209. [CrossRef]
24. Dashora, N.; Taori, A.; Patra, A. Multi-Instrument Observations of Winter-Solstice F Region Irregularities during the Low Solar Activity: New Results and Present Understanding. In Proceedings of the 39th COSPAR Scientific Assembly, Mysore, India, 14–22 July 2012; Volume 39, p. 415.
25. Mohanty, S.; Singh, G.; Carrano, C.; Sripathi, S. Ionospheric Scintillation Observation Using Space-Borne Synthetic Aperture Radar (SAR) Data. *Radio Sci.* **2018**, *53*, 1187–1202. [CrossRef]
26. McNamara, L.F.; Caton, R.G.; Parris, R.T.; Pedersen, T.R.; Thompson, D.C.; Wiens, K.C.; Groves, K.M. Groves Signatures of Equatorial Plasma Bubbles in VHF Satellite Scintillations and Equatorial Ionograms. *Radio Sci.* **2013**, *48*, 89–101. [CrossRef]
27. Woodman, R.F.; La Hoz, C. Radar Observations of F Region Equatorial Irregularities. *J. Geophys. Res. (1896–1977)* **1976**, *81*, 5447–5466. [CrossRef]
28. Whalen, J.A. Equatorial Bubbles Observed at the North and South Anomaly Crests: Dependence on Season, Local Time, and Dip Latitude. *Radio Sci.* **1997**, *32*, 1559–1566. [CrossRef]
29. Pimenta, A.A.; Fagundes, P.R.; Sahai, Y.; Bittencourt, J.A.; Abalde, J.R. Equatorial F-Region Plasma Depletion Drifts: Latitudinal and Seasonal Variations. *Ann. Geophys.* **2003**, *21*, 2315–2322. [CrossRef]
30. Haridas, S.; Unnikrishnan, K.; Choudhary, R.K.; Bose, P.D.; Rao, P.B. A Study on Equatorial Plasma Bubbles over Indian Sub-Continent Using Various Satellite Constellations and Techniques. *AIP Conf. Proc.* **2021**, *2379*, 020003. [CrossRef]
31. Huang, F.; Lei, J.; Xiong, C.; Zhong, J.; Li, G. Observations of Equatorial Plasma Bubbles during the Geomagnetic Storm of October 2016. *Earth Planet. Phys.* **2021**, *5*, eepp2021043. [CrossRef]
32. Kelley, M.C.; Larsen, M.F.; LaHoz, C.; McClure, J.P. Gravity Wave Initiation of Equatorial Spread F: A Case Study. *J. Geophys. Res. Space Phys.* **1981**, *86*, 9087–9100. [CrossRef]
33. Pillat, V.G.; Fagundes, P.R.; Guimarães, L.N.F. Automatically Identification of Equatorial Spread-F Occurrence on Ionograms. *J. Atmos. Sol.-Terr. Phys.* **2015**, *135*, 118–125. [CrossRef]
34. Li, G. Equinoctial and June Solstitial F-region Irregularities over Sanya. *Indian J. Radio Space Phys.* **2012**, *42*, 184.
35. Nakata, H.; Takahashi, A.; Takano, T.; Saito, A.; Sakanoi, T. Observation of Equatorial Plasma Bubbles by the Airglow Imager on ISS-IMAP. *Prog. Earth Planet. Sci.* **2018**, *5*, 66. [CrossRef]
36. Zakharenkova, I.; Cherniak, I. Effects of Storm-Induced Equatorial Plasma Bubbles on GPS-Based Kinematic Positioning at Equatorial and Middle Latitudes during the September 7–8, 2017, Geomagnetic Storm. *GPS Solut.* **2021**, *25*, 132. [CrossRef]

37. Astafyeva, E.; Yasyukevich, Y.V.; Maletckii, B.; Oinats, A.; Vesnin, A.; Yasyukevich, A.S.; Syrovatskii, S.; Guendouz, N. Ionospheric Disturbances and Irregularities During the 25–26 August 2018 Geomagnetic Storm. *J. Geophys. Res. Space Phys.* **2022**, *127*, e2021JA029843. [CrossRef]
38. Mersha, M.W.; Lewi, E.; Jakowski, N.; Wilken, V.; Berdermann, J.; Kriegel, M.; Damtie, B. A Method for Automatic Detection of Plasma Depletions by Using GNSS Measurements. *Radio Sci.* **2020**, *55*, e2019RS006978. [CrossRef]
39. Nishioka, M.; Saito, A.; Tsugawa, T. Occurrence Characteristics of Plasma Bubble Derived from Global Ground-Based GPS Receiver Networks. *J. Geophys. Res. Space Phys.* **2008**, *113*, 1–12. [CrossRef]
40. Nguyen, V.K.; Rovira-Garcia, A.; Juan, J.M.; Sanz, J.; González-Casado, G.; La, T.V.; Ta, T.H. Measuring Phase Scintillation at Different Frequencies with Conventional GNSS Receivers Operating at 1 Hz. *J. Geod.* **2019**, *93*, 1985–2001. [CrossRef]
41. Panda, S.K.; Moses, M.; Ansari, K.; Walo, J. Ionospheric Scintillation Characteristics over Indian Region from Latitudinally-Aligned Geodetic GPS Observations. *Earth Sci. Inform.* **2023**, *16*, 2675–2691. [CrossRef]
42. Vankadara, R.K.; Panda, S.K.; Amory-Mazaudier, C.; Fleury, R.; Devananboyina, V.R.; Pant, T.K.; Jamjareegulgarn, P.; Haq, M.A.; Okoh, D.; Seemala, G.K. Signatures of Equatorial Plasma Bubbles and Ionospheric Scintillations from Magnetometer and GNSS Observations in the Indian Longitudes during the Space Weather Events of Early September 2017. *Remote Sens.* **2022**, *14*, 652. [CrossRef]
43. Zakharenkova, I.; Astafyeva, E.; Cherniak, I. GPS and in Situ Swarm Observations of the Equatorial Plasma Density Irregularities in the Topside Ionosphere. *Earth Planets Space* **2016**, *68*, 120. [CrossRef]
44. Cherniak, I.; Zakharenkova, I.; Sokolovsky, S. Multi-Instrumental Observation of Storm-Induced Ionospheric Plasma Bubbles at Equatorial and Middle Latitudes. *J. Geophys. Res. Space Phys.* **2019**, *124*, 1491–1508. [CrossRef]
45. Huang, C.Y.; Burke, W.J.; Machuzak, J.S.; Gentile, L.C.; Sultan, P.J. Equatorial Plasma Bubbles Observed by DMSP Satellites during a Full Solar Cycle: Toward a Global Climatology. *J. Geophys. Res. Space Phys.* **2002**, *107*, SIA 7-1. [CrossRef]
46. Eastes, R.W.; McClintock, W.E.; Burns, A.G.; Anderson, D.N.; Andersson, L.; Codrescu, M.; Correira, J.T.; Daniell, R.E.; England, S.L.; Evans, J.S.; et al. The Global-Scale Observations of the Limb and Disk (GOLD) Mission. *Space Sci. Rev.* **2017**, *212*, 383–408. [CrossRef]
47. Martinis, C.; Daniell, R.; Eastes, R.; Norrell, J.; Smith, J.; Klenzing, J.; Solomon, S.; Burns, A. Longitudinal Variation of Postsunset Plasma Depletions From the Global-Scale Observations of the Limb and Disk (GOLD) Mission. *J. Geophys. Res. Space Phys.* **2021**, *126*, e2020JA028510. [CrossRef]
48. Cai, X.; Burns, A.G.; Wang, W.; Coster, A.; Qian, L.; Liu, J.; Solomon, S.C.; Eastes, R.W.; Daniell, R.E.; McClintock, W.E. Comparison of GOLD Nighttime Measurements With Total Electron Content: Preliminary Results. *J. Geophys. Res. Space Phys.* **2020**, *125*, e2019JA027767. [CrossRef]
49. Karan, D.K.; Eastes, R.W.; Martinis, C.; Daniell, R.E.; Solomon, S.C.; McClintock, W.E. Unique Combinations of Differently Shaped Equatorial Plasma Bubbles Occurring Within a Small Longitude Range. *ESS Open Arch.* **2023**. [CrossRef]
50. Karan, D.K.; Eastes, R.W.; Daniell, R.E.; Martinis, C.R.; McClintock, W.E. GOLD Mission's Observation About the Geomagnetic Storm Effects on the Nighttime Equatorial Ionization Anomaly (EIA) and Equatorial Plasma Bubbles (EPB) During a Solar Minimum Equinox. *Space Weather* **2023**, *21*, e2022SW003321. [CrossRef]
51. Aa, E.; Zhang, S.-R.; Liu, G.; Eastes, R.W.; Wang, W.; Karan, D.K.; Qian, L.; Coster, A.J.; Erickson, P.J.; Derghazarian, S. Statistical Analysis of Equatorial Plasma Bubbles Climatology and Multi-Day Periodicity Using GOLD Observations. *Geophys. Res. Lett.* **2023**, *50*, e2023GL103510. [CrossRef]
52. Atıcı, R.; Sağır, S. Global Investigation of the Ionospheric Irregularities during the Severe Geomagnetic Storm on September 7–8, 2017. *Geod. Geodyn.* **2020**, *11*, 211–221. [CrossRef]
53. Kassa, T.; Damtie, B. Ionospheric Irregularities over Bahir Dar, Ethiopia during Selected Geomagnetic Storms. *Adv. Space Res.* **2017**, *60*, 121–129. [CrossRef]
54. Huang, C.-S. Continuous Penetration of the Interplanetary Electric Field to the Equatorial Ionosphere over Eight Hours during Intense Geomagnetic Storms. *J. Geophys. Res. Space Phys.* **2008**, *113*, A11305. [CrossRef]
55. Oladipo, O.A.; Adeniyi, J.O.; Olawepo, A.O.; Doherty, P.H. Large-Scale Ionospheric Irregularities Occurrence at Ilorin, Nigeria. *Space Weather* **2014**, *12*, 300–305. [CrossRef]
56. Nayak, C.; Tsai, L.-C.; Su, S.-Y.; Galkin, I.A.; Caton, R.G.; Groves, K.M. Suppression of Ionospheric Scintillation during St. Patrick's Day Geomagnetic Super Storm as Observed over the Anomaly Crest Region Station Pingtung, Taiwan: A Case Study. *Adv. Space Res.* **2017**, *60*, 396–405. [CrossRef]
57. Dugassa, T.; Habarulema, J.B.; Nigussie, M. Longitudinal Variability of Occurrence of Ionospheric Irregularities over the American, African and Indian Regions during Geomagnetic Storms. *Adv. Space Res.* **2019**, *63*, 2609–2622. [CrossRef]
58. Palmroth, M.; Laakso, H.; Fejer, B.G.; Pfaff, R.F., Jr. DE 2 Observations of Morningside and Eveningside Plasma Density Depletions in the Equatorial Ionosphere. *J. Geophys. Res. Space Phys.* **2000**, *105*, 18429–18442. [CrossRef]
59. Kuai, J.; Liu, L.; Liu, J.; Sripathi, S.; Zhao, B.; Chen, Y.; Le, H.; Hu, L. Effects of Disturbed Electric Fields in the Low-Latitude and Equatorial Ionosphere during the 2015 St. Patrick's Day Storm. *J. Geophys. Res. Space Phys.* **2016**, *121*, 9111–9126. [CrossRef]
60. Timoçin, E.; Inyurt, S.; Temuçin, H.; Ansari, K.; Jamjareegulgarn, P. Investigation of Equatorial Plasma Bubble Irregularities under Different Geomagnetic Conditions during the Equinoxes and the Occurrence of Plasma Bubble Suppression. *Acta Astronaut.* **2020**, *177*, 341–350. [CrossRef]

61. Tulasi Ram, S.; Rama Rao, P.V.S.; Prasad, D.S.V.V.D.; Niranjan, K.; Gopi Krishna, S.; Sridharan, R.; Ravindran, S. Local Time Dependent Response of Postsunset ESF during Geomagnetic Storms. *J. Geophys. Res. Space Phys.* **2008**, *113*, A07310. [CrossRef]
62. Sripathi, S.; Banola, S.; Emperumal, K.; Suneel Kumar, B.; Radicella, S.M. The Role of Storm Time Electrodynamics in Suppressing the Equatorial Plasma Bubble Development in the Recovery Phase of a Geomagnetic Storm. *J. Geophys. Res. Space Phys.* **2018**, *123*, 2336–2350. [CrossRef]
63. Brahmanandam, P.S.; Uma, G.; Pant, T.K. Ionosphere VHF Scintillations over Vaddeswaram (Geographic Latitude 16.31° N, Geographic Longitude 80.30° E, Dip 18° N), a Latitude Indian Station—A Case Study. *Adv. Space Res.* **2017**, *60*, 1688–1697. [CrossRef]
64. Tadivaka, R.V.; Paruchuri, B.P.; Miriyala, S.; Koppireddi, P.R.; Devanaboyina, V.R. Detection of Ionospheric Scintillation Effects Using LMD–DFA. *Acta Geophys.* **2017**, *65*, 777–784. [CrossRef]
65. Sridhar, M.; Raju, K.P.; Rao, C.S.; Ratnam, D.V. Mitigation of Ionospheric Scintillations for GPS Signals under Geomagnetic Storm Conditions Using LMS Adaptive Filter. *Int. J. Inf. Commun. Technol.* **2016**, *9*, 389–407. [CrossRef]
66. Ratnam, D.V.; Sivavaraprasad, G.; Lee, J. Automatic Ionospheric Scintillation Detector for Global Navigation Satellite System Receivers. *IET Radar Sonar Navig.* **2015**, *9*, 702–711. [CrossRef]
67. Raghunath, S.; Ratnam, D.V. Detection of Low-Latitude Ionospheric Irregularities From GNSS Observations. *IEEE J. Sel. Top. Appl. Earth Obs. Remote Sens.* **2015**, *8*, 5171–5176. [CrossRef]
68. Vankadara, R.K.; Reddybattula, K.D.; Panda, S.K. Multi-Constellation GNSS Ionospheric Scintillation Monitoring through PolaRx5S Receiver at a Low Latitude Station in India. In Proceedings of the 2021 IEEE International Women in Engineering (WIE) Conference on Electrical and Computer Engineering (WIECON-ECE), Dhaka, Bangladesh, 4–5 December 2021; pp. 184–187.
69. Vankadara, R.K.; Sasmal, S.; Maurya, A.K.; Panda, S.K. An Autoregressive Integrated Moving Average (ARIMA) Based Forecasting of Ionospheric Total Electron Content at a Low Latitude Indian Location. In Proceedings of the 2022 URSI Regional Conference on Radio Science (USRI-RCRS), Indore, India, 1–4 December 2022; pp. 1–4.
70. Vankadara, R.K.; Ratnam Devanaboyina, V.; Panda, S.K. Zonal Irregularity Drift Characteristics of Ionospheric Scintillations from Two Closely-Spaced Global Navigation Satellite System Receivers at an Indian Low Latitude Location. In Proceedings of the 2022 IEEE 11th International Conference on Communication Systems and Network Technologies (CSNT), Indore, India, 23–24 April 2022; pp. 510–514.
71. Vankadara, R.K.; Panda, S.K. Loss of Lock Characteristics of Global Positioning System Signals Under Ionospheric Scintillations at Guntur, India. In Proceedings of the 2023 International Conference on Smart Systems for applications in Electrical Sciences (ICSSES), Tumakuru, India, 7–8 July 2023; pp. 1–4.
72. Yasyukevich, Y.V.; Mylnikova, A.A.; Polyakova, A.S. Estimating the Total Electron Content Absolute Value from the GPS/GLONASS Data. *Results Phys.* **2015**, *5*, 32–33. [CrossRef]
73. Yasyukevich, Y.V.; Mylnikova, A.A.; Kunitsyn, V.E.; Padokhin, A.M. Influence of GPS/GLONASS Differential Code Biases on the Determination Accuracy of the Absolute Total Electron Content in the Ionosphere. *Geomagn. Aeron.* **2015**, *55*, 763–769. [CrossRef]
74. Mylnikova, A.A.; Yasyukevich, Y.V.; Kunitsyn, V.E.; Padokhin, A.M. Variability of GPS/GLONASS Differential Code Biases. *Results Phys.* **2015**, *5*, 9–10. [CrossRef]
75. Seemala, G.K. Chapter 4—Estimation of Ionospheric Total Electron Content (TEC) from GNSS Observations. In *Atmospheric Remote Sensing*; Kumar Singh, A., Tiwari, S., Eds.; Elsevier: Amsterdam, The Netherlands, 2023; pp. 63–84. ISBN 978-0-323-99262-6.
76. Magdaleno, S.; Herraiz, M.; Altadill, D.; de la Morena, B.A. Climatology Characterization of Equatorial Plasma Bubbles Using GPS Data. *J. Space Weather Space Clim.* **2017**, *7*, 12. [CrossRef]
77. Blanch, E.; Altadill, D.; Juan, J.M.; Camps, A.; Barbosa, J.; González-Casado, G.; Riba, J.; Sanz, J.; Vazquez, G.; Orús-Pérez, R. Improved Characterization and Modeling of Equatorial Plasma Depletions. *J. Space Weather Space Clim.* **2018**, *8*, A38. [CrossRef]
78. Aa, E.; Zou, S.; Eastes, R.; Karan, D.K.; Zhang, S.-R.; Erickson, P.J.; Coster, A.J. Coordinated Ground-Based and Space-Based Observations of Equatorial Plasma Bubbles. *J. Geophys. Res. (Space Phys.)* **2020**, *125*, e27569. [CrossRef]
79. Yasyukevich, Y.V.; Kiselev, A.V.; Zhivetiev, I.V.; Edemskiy, I.K.; Syrovatskii, S.V.; Maletckii, B.M.; Vesnin, A.M. SIMuRG: System for Ionosphere Monitoring and Research from GNSS. *GPS Solut.* **2020**, *24*, 69. [CrossRef]
80. Bojilova, R.; Mukhtarov, P. Analysis of the Ionospheric Response to Sudden Stratospheric Warming and Geomagnetic Forcing over Europe during February and March 2023. *Universe* **2023**, *9*, 351. [CrossRef]
81. Lan, T.T.; Fleury, R.; Amory-Mazaudier, C.; Thang, N.C.; Thanh, N.H. TEC Variations and Ionospheric Disturbances during the Magnetic Storm in March 2015 Observed from Continuous GPS Data in the Southeast Asia Region. *Vietnam J. Earth Sci.* **2016**, *38*, 267–285. [CrossRef]
82. Alves, M.V.; Echer, E.; Gonzalez, W.D. Geoeffectiveness of Corotating Interaction Regions as Measured by Dst Index. *J. Geophys. Res. Space Phys.* **2006**, *111*, A07S05. [CrossRef]
83. Fejer, B.G. Effects of the Vertical Plasma Drift Velocity on the Generation and Evolution of Equatorial Spread F. *J. Geophys. Res. Space Phys.* **1999**, *104*, 19859–19869. [CrossRef]
84. Biktash, L.Z. Role of the Magnetospheric and Ionospheric Currents in the Generation of the Equatorial Scintillations during Geomagnetic Storms. *Ann. Geophys.* **2004**, *22*, 3195–3202. [CrossRef]
85. Tsurutani, B.; Mannucci, A.; Iijima, B.; Abdu, M.A.; Sobral, J.H.A.; Gonzalez, W.; Guarnieri, F.; Tsuda, T.; Saito, A.; Yumoto, K.; et al. Global Dayside Ionospheric Uplift and Enhancement Associated with Interplanetary Electric Fields. *J. Geophys. Res. Space Phys.* **2004**, *109*, A08302. [CrossRef]

86. Liu, Y.; Fu, L.; Wang, J.; Zhang, C. Studying Ionosphere Responses to a Geomagnetic Storm in June 2015 with Multi-Constellation Observations. *Remote Sens.* **2018**, *10*, 666. [CrossRef]
87. Hussien, F.; Ghamry, E.; Fathy, A. A Statistical Analysis of Plasma Bubbles Observed by Swarm Constellation during Different Types of Geomagnetic Storms. *Universe* **2021**, *7*, 90. [CrossRef]
88. Rama Rao, P.; Gopi Krishna, S.; Niranjan, K.; Prasad, D. *Study of Spatial and Temporal Characteristics of L-Band Scintillations over the Indian Low-Latitude Region and Their Possible Effects on GPS Navigation*; Copernicus GmbH: Göttingen, Germany, 2006; Volume 24, pp. 1567–1580.
89. Yang, Z.; Morton, Y.T.J. Low-Latitude GNSS Ionospheric Scintillation Dependence on Magnetic Field Orientation and Impacts on Positioning. *J. Geod.* **2020**, *94*, 59. [CrossRef]
90. Magdaleno, S.; Herraiz, M.; de la Morena, B.A. Characterization of Equatorial Plasma Depletions Detected from Derived GPS Data in South America. *J. Atmos. Sol.-Terr. Phys.* **2012**, *74*, 136–144. [CrossRef]
91. Deng, B.; Huang, J.; Kong, D.; Xu, J.; Wan, D.; Lin, G. Temporal and Spatial Distributions of TEC Depletions with Scintillations and ROTI over South China. *Adv. Space Res.* **2015**, *55*, 259–268. [CrossRef]